


## Interaction of low aspect ratio, cantilevered, chamfered cylindrical pins with a laminar boundary layer

Tomás E. Rojas Carvajal  and Michael Amitay \*

*Department of Mechanical, Aerospace and Nuclear Engineering Engineering, Rensselaer Polytechnic Institute, 110 8th St, Troy, New York 12180, USA*

Tufan Kumar Guha 

*Department of Aerospace Engineering, Indian Institute of Technology Kanpur, Kanpur 208016, India*



(Received 26 December 2022; accepted 7 April 2023; published 22 May 2023)

The flow field associated with cantilevered, low aspect ratio cylindrical pins having different chamfered free-ends were investigated using oil flow visualizations and stereoscopic particle image velocimetry at  $Re_D = 8 \times 10^3$ . Two chamfered pins, where the chamfer encompassed either half of the pin's planform or its full planform, were analyzed with the chamfer at various skew angles with respect to the freestream and were compared with a pin without a chamfer. All pins exhibited a complex flow field, including an array of streamwise vortical structures. The chamfered pins resulted in two additional counter-rotating streamwise vortices, named chamfered induced vortices (CIVs). It was shown that changing the skew angle resulted in a change in the strength of these vortical structures, their direction of rotation, and as a result, the net circulation produced. Comparing the two chamfered pins, the pin where the chamfer encompassed half of its planform produced stronger CIVs. These effects are discussed in detail to provide insight into a future use of these pins as flow control devices.

DOI: [10.1103/PhysRevFluids.8.054701](https://doi.org/10.1103/PhysRevFluids.8.054701)

### I. INTRODUCTION

The subject of flow past finite-span, cantilevered cylinders immersed in a boundary layer has been investigated by multiple studies that show the complex, three-dimensional flow field that they produce. It must be noted that as flow control devices, these cantilevered cylinders are commonly small-scale and thus sometimes referred to as pins. In the present work, these two terms will be regarded as equivalent. The most notable difference compared with the two-dimensional cylinder is that the flow is significantly influenced by the downwash entrained over the free end of the cylinder, which interacts with the near wake [1]. The interaction between this downwash and the near wake has been found to be predominantly dependent upon the Reynolds number and the aspect ratio [2]. Sakamoto and Arie [3] explored the interactions of finite prisms and cylinders with turbulent boundary layers by using the smoke-wire method and observed that two types of vortices were formed behind the body. They found that, for cylinders with aspect ratio smaller than 2.5, arch-type vortices are formed in their wake. However, cylinders with aspect ratio greater than 2.5 produced alternating von Kármán-type vortices, more commonly associated with the flow behind a two-dimensional cylinder. This change in the observed structure was described as a decay in the peak ratio of the prominent frequency as recorded by a hot wire and was accompanied by a change in the slope of the variation of the associated Strouhal number with aspect ratio. They found that

---

\*amitam@rpi.edu

the slope of the Strouhal number versus aspect ratio behaved approximately in a piecewise linear fashion, with a steeper slope below aspect ratio of 2.5 and a shallower slope for greater aspect ratios.

Kawamura *et al.* [4] further characterized the flow field behind the cylinders at aspect ratios below and above this critical aspect ratio  $AR_c$  using pressure ports along the side of the cylinders. They observed that, in general, the isopressure coefficient lines on the cylindrical surface were approximately parallel to the cylinder long axis on the upstream portion of the cylinder wall, with the notable exception of both ends of the pin where pressure drops were observed; the pressure drop at the root of the cylinder (a consequence of the boundary layer) being smaller than that at the free end. At the free end, Kawamura *et al.* postulated that the upwash flow separated at an oblique angle to the leading edge. This separated flow interacted with the downwash over the pin, forming a pair of trailing vortices. This was contradicted by Holscher and Niemann [5] who showed bending of separation lines on the sides of the cylinder, the mean recirculation zone on the free-end surface containing a cross-stream (mushroom like) vortex, and the streamwise tip vortices originating from the sides of the cylinder on the edge of the free end. Furthermore, Kawamura *et al.* [4] found that, for larger aspect ratio cylinders, the region, where the isopressure lines are parallel to the cylinder axis, behaves similar to the case for a two-dimensional cylinder. As the aspect ratio becomes smaller, it is this region that gets shorter while the pressure drops at either end stay approximately the same. Thus, the formation of vortex streets is suppressed near the free end of the cylinder by the downwash entrained over the free end.

While the flow behavior described above is universally recognized, the value of the critical aspect ratio has been found to vary greatly in the range  $1 \leq AR_c \leq 7$  [6]. As mentioned before, Kawamura *et al.* [4] found it to be approximately four, a result also observed by Okamoto and Sunibashiri [7]. However, the former also noted that the value of the critical aspect ratio increases with the thickness of the incoming boundary layer  $\delta$ . Other studies have also noted a similar dependency, more commonly expressed in terms of a dimensional immersion ratio  $h/\delta$ , where  $h$  is the pin's height. These include Sakamoto and Arie [3], Palau-Salvador *et al.* [8], and Gildersleeve & Amitay [1,9]. Additionally, Fox and West [10] explored cantilevered cylinders with aspect ratios of 4 and 30 and found that beyond the aspect ratio of 13, the mean pressure distributions, pressure drag, and spanwise variations of the Strouhal number became independent of the aspect ratio.

Pattenden, Turnock, and Zhang [11] used surface flow visualization, particle image velocimetry (PIV), and surface pressure measurements to observe the flow over a finite span cylinder of aspect ratio 1 at a diameter-based Reynolds number  $Re_D$  of 200 000. They divided the flow field into three distinct regions: the horseshoe vortex system, the separated flow over the cylinder's free-end which included an arch vortex, and the wake region; thus noting that this aspect ratio is subcritical. They also pointed out that the wake region was found to be highly unsteady, with a large variation of the instantaneous velocity fields from the mean flow.

Despite this spread in the results in the literature regarding the critical aspect ratio, low aspect ratio pins, defined as those with aspect ratio smaller than 1, such as those used by Gildersleeve and Amitay [1,9], Gildersleeve *et al.* [12,13], Shehata and Medina [14], or the present study, can safely be thought of as being well within the aspect ratio range where symmetric arch-type shedding is present. Thus, studies such as the aforementioned Kawamura *et al.* [4], Gildersleeve and Amitay [1], Gildersleeve [15], Roh and Park [16], Holscher and Niemann [5], or Shehata and Medina [14], are of particular importance for the present paper. Such studies have shown that these flows are highly three-dimensional [1] and that the flow over the free end of these cylinders has several features which are shown in Fig. 1(a), adapted from Gildersleeve and Amitay [1]. The flow topology on the top of the free end of the pin shows the presence of two foci, denoted  $F$ , in the upstream half of the pin. These foci are associated with a cellular mushroom-type vortex that is formed due to flow separation. In the downstream half of the pin's free end there are two nodes,  $N$ , from which the two tip vortices originate and subsequently enter the wake. Since the flow field is symmetrical, two saddle points  $S$  exist between these two pairs of features. Additionally, the study by Gildersleeve and Amitay [1] also showed that the flow past a cylindrical pin, which was immersed in a laminar boundary layer, is composed of several flow features. They found that the locations and strengths

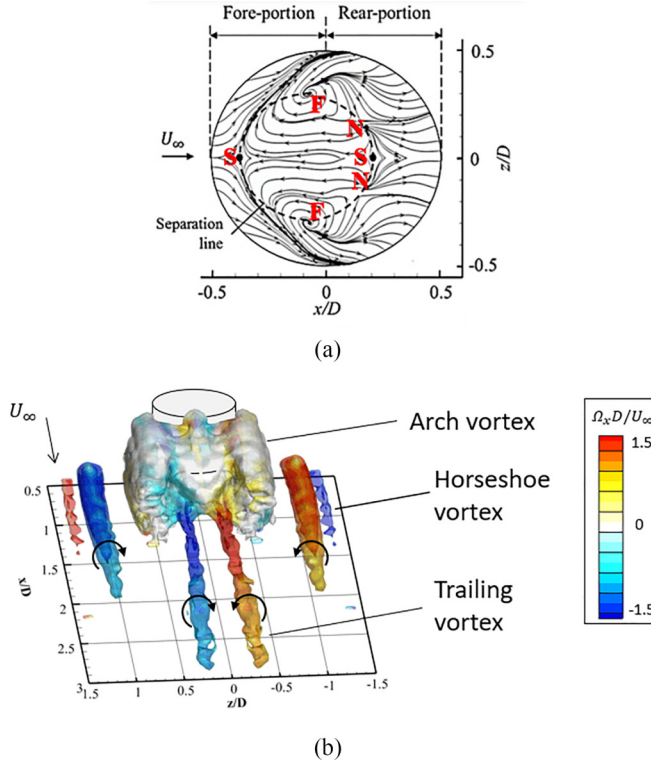


FIG. 1. (a) Near-surface streamlines from *SPIV* measurements over a low aspect ratio, cantilevered pin, adapted from Gildersleeve and Amitay [1]. The labels indicate locations of certain features, *F*: Foci, *S*: Saddle Points, *N*: Nodes. (b) Isosurfaces of normalized  $Q$ , colored by normalized streamwise vorticity, showing the main features seen in the flow past a low aspect ratio, cantilevered pin. Reprinted from Gildersleeve [15].

of these features depend on the aspect ratio of the pin and its immersion ratio  $h/\delta$ . These features are illustrated as isosurfaces of normalized  $Q$ , colored by streamwise vorticity, in Fig. 1(b), which is reprinted from Ref. [15]. Symmetrical pairs of horseshoe vortices develop around the periphery of the pin, which are products of the three-dimensional boundary layer separation in the region of adverse pressure gradient immediately upstream of the cylinder. The separated boundary layer rolls into a vortex and is swept around the base of the cylinder [17–19]. The flow around the sides of the pin interacts simultaneously with the separated flow over the pin’s free end to form the arch vortex, and with the horseshoe vortices to develop into streamwise vortices downstream of the pin. This second effect is limited to the downwash portion of the side flow as noted by Kawamura *et al.* [4]. A recirculation region is formed in the wake due to the flow separation over the free end, downstream of the recirculation region a pair of counter-rotating trailing vortices can also appear in the wake.

Using the information gathered about the flow field behind the low aspect ratio cylinders, studies such as Gildersleeve *et al.* [13] (dynamic pins) and Shehata & Medina [14] (rotating pins) investigated the ability to change the flow field around them with the ulterior objective of using such cylinders as flow control devices. In that sense, a modified version of these pins could improve certain vorticity-inducing capabilities and be more effective at specific flow control tasks. With this background, the present study explores the flow field downstream of a low aspect ratio, cantilevered cylindrical pins which do not have a rectangular frontal cross section. In these modified pins, the entirety or a portion of the pin’s free end is chamfered. The interaction of these chamfered pins with

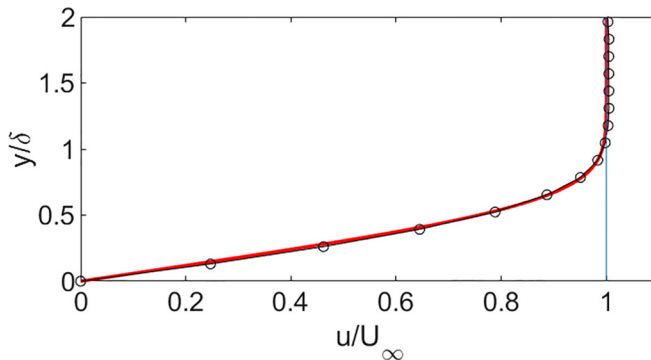


FIG. 2. Comparison of the experimental boundary layer profile (symbols), extracted at the location of pin mounting, with the Blasius solution (red line).

a laminar boundary layer is explored where the chamfered free end is oriented at different azimuth angles with respect to the freestream.

## II. EXPERIMENTAL SETUP

The experiments were conducted in the small-scale, low-speed wind tunnel facility at the Center for Flow Physics and Control (CeFPaC) at Rensselaer Polytechnic Institute. The tunnel is open-return and suction-based with a test-section that is 610 mm long and has cross-sectional dimensions of 101.6 mm  $\times$  101.6 mm. The inlet area contraction ratio is 9 : 1 with a length-to-diameter ratio of 1.5. Series of honeycombs and screens, located upstream of the contraction, result in a turbulence level of less than 0.5%. Three walls of the test section are made from acrylic to allow optical access. The tunnel is operated using a three-bladed turbine blower connected to a 5 HP AC motor and a variable frequency drive. All present experiments were conducted at a freestream velocity of 10 m/s. The corresponding Reynolds number, based on the pin diameter ( $D = 12$  mm), is  $Re_D = 8 \times 10^3$ , and the corresponding Reynolds number, based on the local boundary layer thickness at the location of the pin ( $\delta = 3$  mm), is  $Re_\delta = 2 \times 10^3$ . To confirm that the incoming flow is laminar, the boundary layer profile at the location of the pin (in the absence of the pin) was extracted from the mean *SPIV* flow field and compared with the Blasius solution (Fig. 2). The agreement between the profiles shows that the flow is laminar with a shape factor of  $H = 2.6$ .

### A. Test models

Three cylindrical pins were analyzed in the study, all with a common diameter of  $D = 12$  mm. The pins were machined from 6061 aluminum and designed to protrude 4 mm ( $h/\delta = 1.3$ ,  $AR = h/D = 0.33$ ) into the flow when mounted to the test-section floor. The immersion and aspect ratios were chosen to help achieve sufficient downwash and arch-type shedding respectively according to results from the literature (specifically, Gildersleeve and Amitay [1] and Gildersleeve *et al.* [13]). The first pin [Fig. 3(a)] has no chamfer and was used as a baseline for comparison with the chamfered pins. The full-chamfered pin [Fig. 3(b)] has an edge-to-edge slanted top plane, whereas for the half-chamfered pin [Fig. 3(c)] only half of the top surface is slanted.

In both chamfered pins, the height difference between the highest and lowest point of the slanted plane is 1.5 mm ( $0.5\delta$ ). The value of this difference is intended such that the highest and lowest point of the slanted plane straddle the boundary layer thickness and thus encounter a difference in the incoming velocity, and is kept constant to aid comparison. The height requirements and the diameter determine the angles of the slopes. The resultant angle of the slope is  $7.125^\circ$  for the full-chamfered pin and  $14.04^\circ$  for the half-chamfered pin.

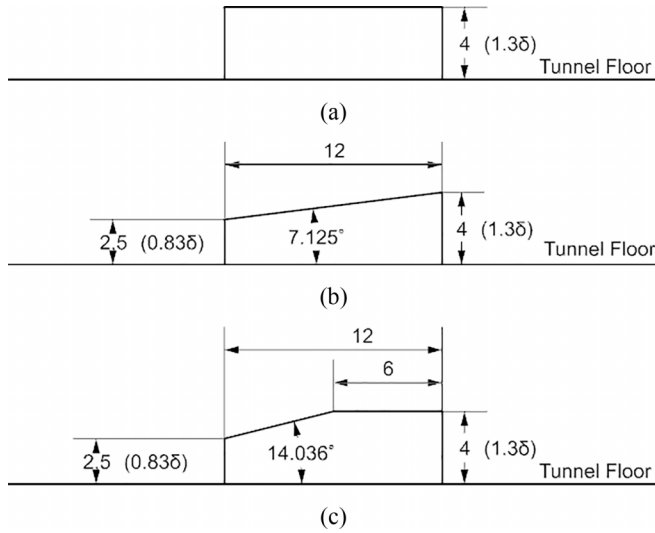


FIG. 3. Schematics of (a) baseline, (b) full-chamfered, and (c) half-chamfered pins mounted on the wind tunnel floor. All dimensions are in mm. In the current sketch the chamfer skew angle is  $\phi = 90^\circ$  and the flow is out of the page.

The pins were placed in a circular cutout on the tunnel floor, centered at 200 mm downstream of the inlet plane, using a circular insert. The insert could be rotated to set the chamfer at different skew angles,  $\phi$ , with respect to the freestream. To explore the effects of  $\phi$  on the chamfered pins, the skew angle was varied from a position where the slanted plane was forward-facing with respect to the flow ( $\phi = 0^\circ$ ) to the position where it was backward facing with respect to the flow ( $\phi = 180^\circ$ ). The skew angle was changed by increments of  $45^\circ$  as shown in Fig. 4.

The origin of the coordinate system in this study is located at the intersection between the centerline of the pin and the floor plane, with the  $x$  axis in the streamwise direction, the  $y$  axis normal to the floor, and the  $z$  axis in the spanwise direction. It should be noted that the positive  $z^*$  direction is towards the left when looking upstream, towards the chamfer. These coordinates were

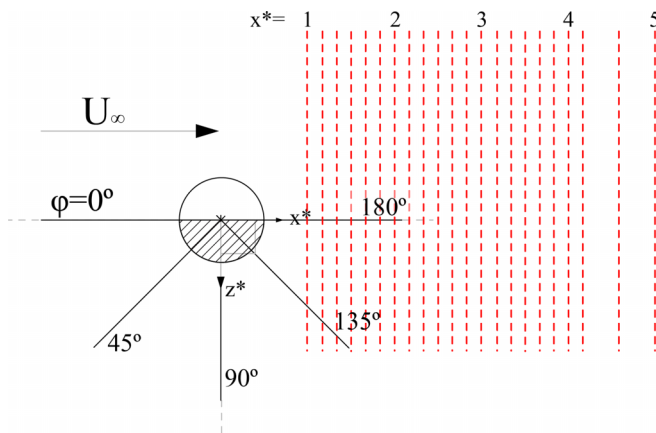


FIG. 4. Skew angles and spanwise planes used for *SPIV* data collection. The shaded portion represents the half-chamfer. Here, the chamfer is at  $\phi = 90^\circ$ .

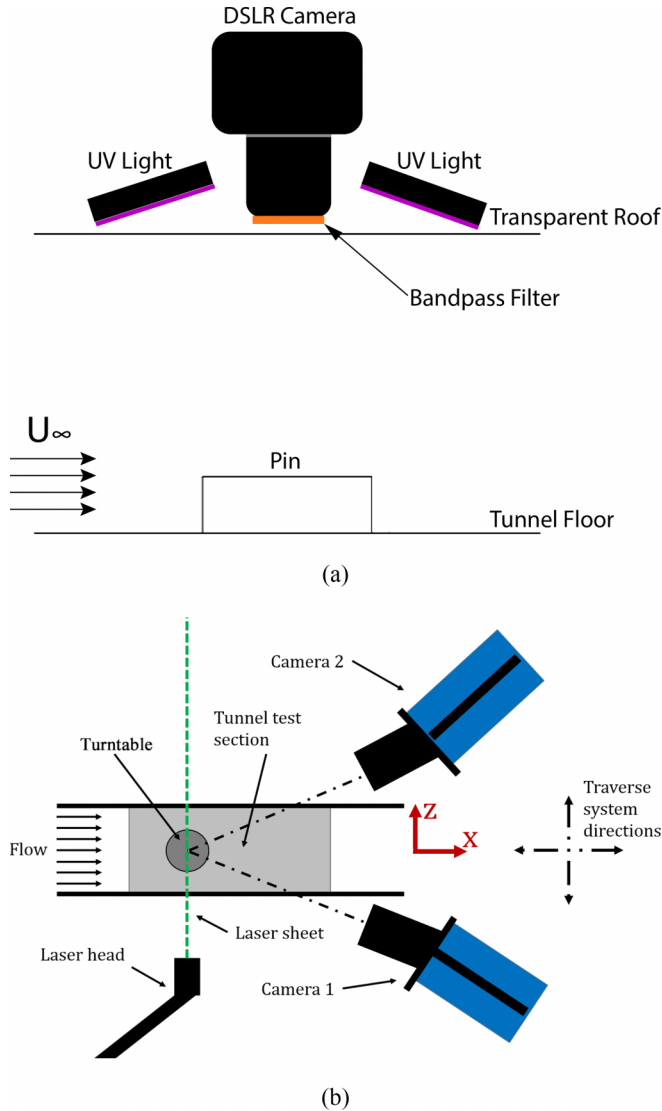


FIG. 5. Diagrams of the setups for (a) *OFV*, and (b) *SPIV* measurements in the wind tunnel. Not to scale.

rendered dimensionless using the pin diameter  $D$  to give the nondimensional coordinates  $x^*$ ,  $y^*$ , and  $z^*$ , respectively.

## B. Measurement techniques

The flow field was first qualitatively observed using surface topology via oil flow visualization (*OFV*). A schematic of the experimental setup is shown in Fig. 5(a). This was done by manually applying a thin film of a 20 : 1 mix of silicone oil (20 cst) and a florescent tracer using a paintbrush over and around the pin. The tunnel was then illuminated with ultraviolet LED arrays and images were taken using a Canon EOS 77D digital single lens reflex camera (DSLR) equipped with a 35–105 mm multifocal lens and a 550 nm low-pass filter. The images were taken every 10 seconds until a steady state was reached. The steady-state flow field images for different cases are presented in the results section (with inverted colors to increase contrast).

Additionally, the flow field downstream of the pin, starting at  $x^* = 1$ , was measured using stereoscopic particle image velocimetry (*SPIV*). This initial value of  $x^*$  was selected to avoid obstructions and reflections from the pin. A schematic of the experimental setup for *SPIV* is shown in Fig. 5(b).

Measurements were conducted at downstream locations spanning from  $x^* = 1$  to  $x^* = 4.2$  at increments of  $x^* = 0.167$  (2 mm), and from  $x^* = 4.6$  to  $x^* = 5$  at increments of  $x^* = 0.4$  (5 mm), the locations are shown as dashed red lines in Fig. 4. In the region close to the pin ( $0 \leq x^* \leq 1$ ) data could not be acquired due to glare from the pin when the flow was illuminated. The flow was seeded using water-based particles with diameters in the order of  $1 \mu\text{m}$ . The particles were illuminated using a 120 mJ New Wave Nd:YAG double pulsed laser. The incident ray was focused using an adjustable focal lens (focal length from 500 to 3000 mm) and fanned into a sheet using a cylindrical lens (radius of  $-50$  mm). The thickness of the laser sheet in the interrogation window was approximately 2 mm. Images were acquired using two 2-megapixel LaVision Imager Pro 2M CCD cameras. Each camera was fit with a 105 mm Nikon lens and a Scheimpflug adapter. The laser and the cameras were mounted on computer-controlled traverses, allowing movement along the axis of the flow. This helped in preserving the camera calibration at different downstream locations. However, *SPIV* self-calibration was still conducted at each plane to remove misalignment between the laser and the cameras. For each case, 500 image pairs were acquired at 10 Hz, and processed using LaVision Davis 8.4.0 software, where vector processing was performed using a multipass decreasing size algorithm. The initial window size was  $64 \times 64$  pixels with 50% overlap and the final window size was  $32 \times 32$  pixels with 50% overlap. The final vector resolution is 0.2 mm (0.0167D or 0.067 $\delta$ ). On average, fewer than 10 pixels were removed by the software after processing each instantaneous image, which constitutes less than 0.05% of the 180-by-119 pixel final image size. The mean and standard deviation of the corresponding processed vector fields were used to obtain the time-averaged flow field and the turbulent kinetic energy field, *TKE*, respectively.

Uncertainty quantification was obtained directly from DaVis, which uses the method proposed by Weineke [20]. The mean uncertainty of  $u/U_\infty$  over the 500 instantaneous uncertainty fields is shown in Fig. 6, the data corresponds to a representative plane located at  $x/D = 3$  (approximately the center of the measurement domain) for the baseline (nonchamfered) pin case. In this representative plane, the average uncertainty of the out of plane component is 1.22% with a maximum of 3% occurring near the surface. As expected, the in-plane velocities have smaller uncertainty values, with peak values under 2%. Comparable uncertainty levels were observed in all planes investigated.

The uncertainty of the *TKE* was calculated following the derivations of Sciacchitano and Wieneke [21] using the following equation:

$$\zeta_{TKE} = \frac{1}{2N} * \sqrt{(\overline{u'})^2 + (\overline{v'})^2 + (\overline{w'})^2}, \quad (1)$$

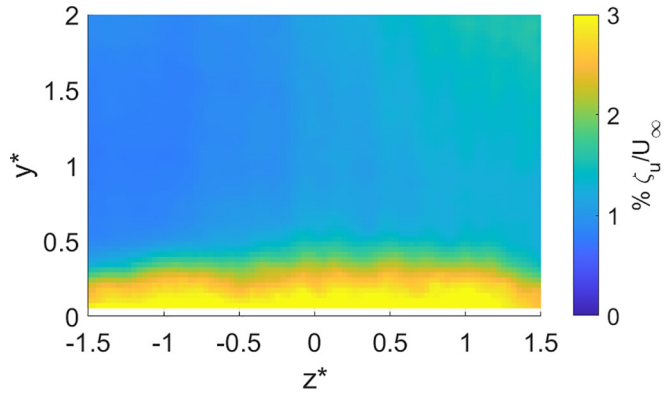
where  $N$  is the number of samples. Based on these derivations, the maximum uncertainty of the *TKE* in the wake of the pin was about 5%.

### C. Vortex identification method

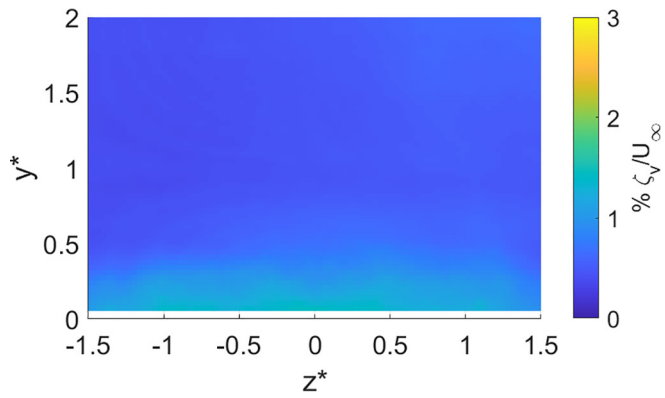
The  $Q$  criterion was used in each data plane to identify the vortices, whereas their direction of rotation was identified using the streamwise vorticity. The in-plane  $Q$  was calculated as shown:

$$Q = -\frac{1}{2} \left[ \left( \frac{\partial w}{\partial z} \right)^2 + \left( \frac{\partial v}{\partial y} \right)^2 \right] - \frac{\partial w}{\partial y} \frac{\partial v}{\partial z}. \quad (2)$$

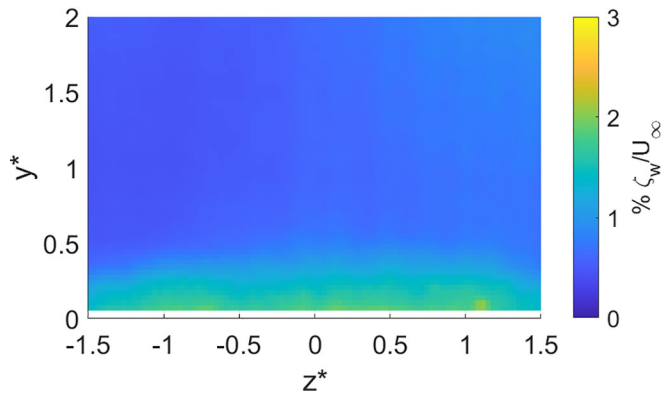
The streamwise component of the circulation,  $\Gamma_x$ , of the vortices was then obtained by integrating the streamwise vorticity inside the regions enclosed by the contour lines corresponding to 10% of the peak vorticity. Additionally, MATLAB clustering algorithms were used to distinguish between the multiple observable vortices and identify their geometric centroids. The centroids were used for calculating the downstream trajectories of these vortices.



(a)



(b)



(c)

FIG. 6. Percentage of uncertainty of the normalized velocity components, (a)  $\zeta_u/U_\infty$ , (b)  $\zeta_v/U_\infty$ , and (c)  $\zeta_w/U_\infty$ , at a plane located at  $x^* = 3$ . Flow is out of the page.



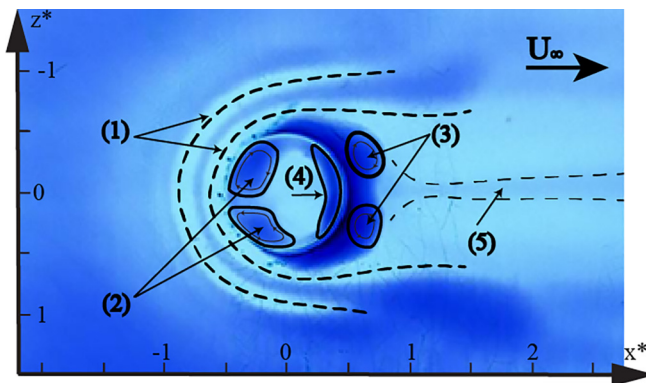


FIG. 7. Surface topology for the baseline pin using oil flow visualization. The overlaid sketches and numerical annotations represent several features of the surface topology: (1) two sets of horseshoe vortices, (2) cellular mushroom-type vortex foci, (3) arch vortex legs, (4) second detachment of the boundary layer at the trailing edge associated with the arch vortex, and (5) oil accumulation between the two trailing vortices.

### III. RESULTS

The results section presents data from the *OFV* and the *SPIV* campaigns. The *OFV* results are discussed first and allow qualitative evaluation of the flow features in the vicinity of the pin, including the region directly upstream of the pin, over the pin, and the near field downstream of it. This is important because, when performing *SPIV*, some portions of these regions are obstructed by the pin itself and by reflections of the laser on the pin. The *SPIV* results are discussed after the *OFV* results and focus on the evolution of the vortices downstream of the near field and their interactions.

#### A. Oil flow visualization

First, the results corresponding to the *OFV* are discussed. For the baseline pin (i.e., no chamfer), the main flow features, as were discussed by Gildersleeve and Amitay [1], can be seen in Fig. 7. Here,  $Re_D = 8 \times 10^3$ ,  $h/\delta = 1.33$ , and  $AR = 0.33$ . The surface topology shows evidence of three sets of horseshoe vortices. This includes one that is weak and two that are much more prominent, which are indicated as (1). Additionally, two large oil concentrations, indicated as (2), are present on upper surface of the pin near its leading edge, one on each side of the symmetry line. These correspond to the local flow separation and the formation of the cellular mushroom-type vortex over the free end. This feature was also observed by previous studies such as by Roh and Park [16] who called them “eye-like shapes,” and by Gildersleeve and Amitay [1]. This cellular separation bubble reattaches over the free end of the pin, then separates again at the trailing edge to form the arch vortex, as was shown by Refs. [1,22]. The vortex causes the concavity in the oil accumulation around the centerline, indicated as (3), as its “legs” reach the surface. The indicated directions of rotation in (2) and (3) are based on the results by Gildersleeve and Amitay [1]. The second detachment of the boundary layer at the trailing edge of the free end generates the oil concentration seen in that region, indicated as (4). Finally, a single streak of oil extends downstream past the near wake, between the two trailing vortices, indicated as (5).

Next, the *OFV* results for the chamfered pins at different skew angles are discussed and presented in Fig. 8. The images in the figure are laid out in a grid with each row showing a different skew angle and each column corresponding to a particular pin. The oil concentrates at the locations of minimum shear of the surface topology and thus indirectly traces the different vortices. For the chamfered pins, the size and locations of the different flow features depend on the shape of the pin itself and the skew angle with respect to the flow. However, it must be noted, that in all cases there is similar behavior of the horseshoe vortices (noted as 1) upstream of the pin. Since the horseshoe vortices are formed

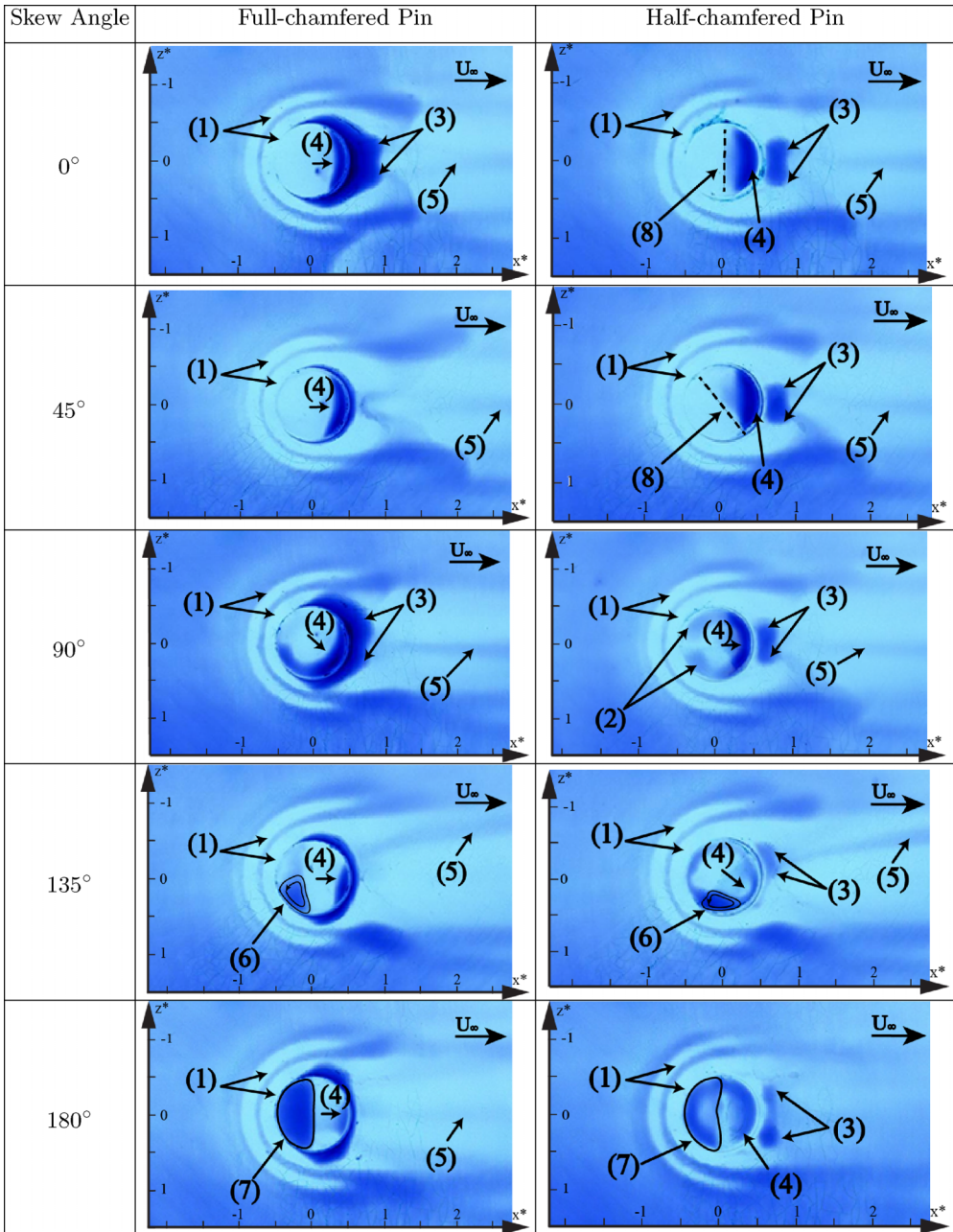


FIG. 8. Oil flow visualizations for the two chamfered pins at different skew angles. The numerical annotations denote several features of the surface topology: (1) two sets of horseshoe vortices, (2) cellular mushroom-type vortex foci, (3) possible arch vortex legs, (4) second detachment of the flow at the trailing edge associated with the arch vortex, (5) oil accumulation between the two trailing vortices, (6) asymmetric separation cell, (7) symmetric leading-edge separation bubble, and (8) separation line at the end of the chamfered portion of the pin. Features not seen in the baseline pin have overlaid sketches. Flow is from left to right.

by the roll-up of the separated boundary layer around the base of the cylinder [1], this suggests that the boundary layer in this region is relatively unaffected by the geometry of the free end. Therefore, since all other conditions are the same, the differences in the downstream behavior of the flow must, whether directly or indirectly, be a consequence of the interaction of the different free ends with the higher-momentum fluid in the freestream (since the height of the pins is  $1.3\delta$ ).

At  $\phi = 0^\circ$ , both chamfered pins produce arch vortices (noted by the oil concentrations at 3) that are smaller in the spanwise direction than the one produced by the baseline pin. Additionally, the *OFV* suggests a change in the angle at which the horseshoe vortices detach from the cylinder surface, which is responsible for the smaller arch vortices. The chamfer also suppresses the formation of the cellular mushroom-type vortex at the leading edge of the free end as is suggested by the absence of corresponding oil concentrations. The separation is replaced by a region of high shear due to the interaction of the incoming flow with the chamfer. In the case of the full-chamfered pin, this high shear region occupies almost the entire free end and only a small oil concentration (noted as 4), corresponding to the separation of the flow into the arch vortex (as seen by Gildersleeve and Amitay [1] for a nonchamfered pin). For the half-chamfered pin, however, separation occurs over the sharp edge between the chamfered and nonchamfered portions (8), yielding a larger oil accumulation near the trailing edge. Lastly, similar oil lines can be observed between the two trailing vortices (5) for both the full-chamfered and the half-chamfered pin.

When the full-chamfered pin is rotated to  $\phi = 45^\circ$ , the legs of the arch vortex are not distinguishable. Additionally, the symmetry is lost, evinced by the oil accumulation at the trailing edge (4) of the pin, as well as the asymmetry of the oil lines corresponding to the interaction between the arch vortex and the first horseshoe. The downstream effect of this asymmetry is that the trailing vortices are slightly asymmetric. This asymmetry of the trailing vortices is also present, and more noticeable, for the half-chamfered pin at  $\phi = 45^\circ$ . This is accompanied by a larger asymmetry in the arch-horseshoe interaction. On the free end of the pin, the separation line seen at the sharp edge between the chamfered and nonchamfered portions (8) is now oblique to the flow. This asymmetric separation is not present on the full-chamfered pin and seems to enhance the asymmetry of the flow field downstream.

At  $\phi = 90^\circ$ , the chamfer surfaces are no longer facing towards the flow, which eliminates the high-pressure regions on them. On the full-chamfered pin, the oil accumulates around the periphery of the chamfer surface, concentrated around the lower end of the chamfer surface ( $z^* > 0$ ) and the trailing edge (4). This suggests a combined effect of the separation around the circular edge of the pin and the asymmetric arch vortex, which can also be seen. The asymmetry of the arch vortex is due to the different heights of the cylindrical surface at its spanwise extremes. The oil line between the trailing vortices (5) is angled towards the side that has the chamfer and becomes more diffuse downstream as the trailing vortices decay. The half-chamfered pin shows oil concentrations over the free end that are similar to those of the baseline pin, with evidence of a similar cellular mushroom-type vortex (2) on the two surfaces and the oil concentrations (4) produced by the arch vortex. Downstream of the pin, the oil concentrations, corresponding to the legs of the arch vortex (3), are shifted away from the chamfer. As with the full-chamfered pin, the oil line between the trailing vortices is angled towards the side of the pin containing the chamfer and becomes more diffuse downstream as the trailing vortices decay.

At  $\phi = 135^\circ$ , on the pins' free end, the chamfer surface is now on the wake side, albeit at an angle. On the full-chamfered pin, an oil concentration can be seen near the leading edge as the flow separates around the highest point of the chamfer and rolls up (noted as 6). Since the flow separates around a sharp edge, this structure rotates in the direction that is sketched. The arch vortex itself is difficult to assess. However, there is still a visible concentration of oil on the trailing edge towards the lowest point of the chamfer surface, similar to that caused by the arch vortex on the previous images. Interestingly, the angle of the oil line between the two trailing vortices dramatically shifts away from the side of the pin that has the chamfer (noted as 5), suggesting that the trailing vortex on the side that is away from the chamfer merges with the horseshoe vortex; this will be shown in the *SPIV* results. Additionally, the entire system of horseshoe vortices on this side unwraps

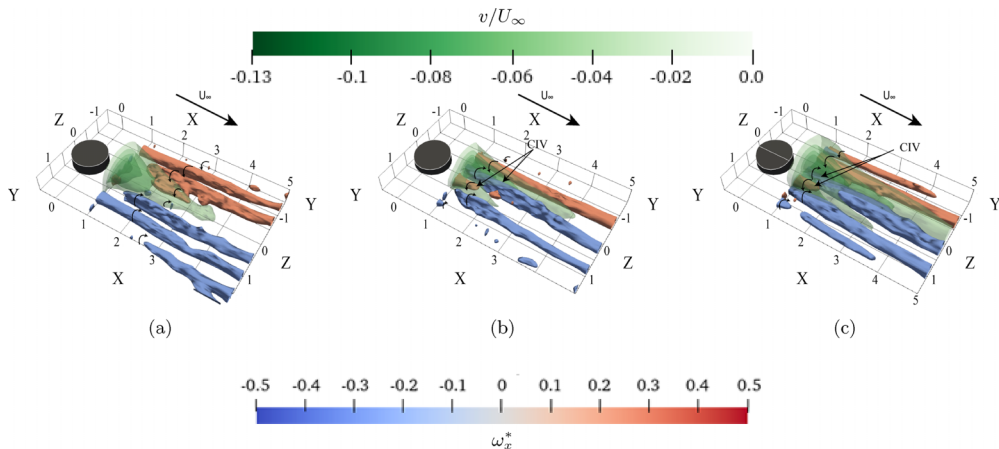


FIG. 9. Isosurfaces of normalized  $Q$  ( $Q = 0.012$ ), colored by normalized streamwise vorticity, superimposed with color contours of normalized vertical velocity for the baseline pin (a), full-chamfered pin (b), and half-chamfered pin (c). In both chamfered pins  $\phi = 90^\circ$ .

slightly from the pin circumference and angles away from the pin. On the half-chamfered pin, a concentration of oil can be seen near the point of the chamfer that is highest and farthest upstream, which is similar to that for the full-chamfered pin. The legs of the arch vortex are close together and at an angle from the freestream. The oil line between the trailing vortices arches away from the side that has the chamfer, similar to the full-chamfered pin.

Finally, at  $\phi = 180^\circ$ , the oil topology is again symmetric, as expected. On the free end of the full-chamfered pin, there is a large oil concentration near the pin's leading edge at the tip of the chamfer (7), corresponding to a separation bubble. Additionally, the smaller oil concentration is also present (4), which is very small on the full-chamfered pin. The half-chamfered pin presents a clearer arch vortex, with its legs farther apart than for the previous skew angles. Moreover, the oil concentration on the free end of the pin corresponds to flow separation at the leading edge. However, there is no clear evidence of a cellular mushroom-type vortex and most of the free end surface has some oil accumulation, suggesting the chamfered half, which is at the aft section of the pin, delays reattachment of the flow over the pin and suppresses the formation of the mushroom vortex.

This concludes the section on *OFV* visualization, which serves to provide qualitative insight and context to the quantitative data from the *SPIV* campaign, which is discussed in the following section.

## B. Stereoscopic particle image velocimetry

For the *SPIV* results, the baseline (nonchamfered) pin is described first and serves as a comparison with the chamfered pins. Then, the two chamfered pins are presented at a fixed skew angle of  $\phi = 90^\circ$  and compared. The effect of each pin on the surrounding flow field is analyzed. Subsequently, the effect of the chamfer skew angle on the formation and interaction of the vortical structures is analyzed for the half-chamfered pin.

### 1. Comparison between the different pin geometries

Figure 9 shows isosurfaces of normalized  $Q$  ( $Q = 0.012$ ), colored by normalized streamwise vorticity  $\omega_x^*$ , and superimposed with isosurfaces of  $v/U_\infty$  ( $v/U_\infty = -1.25, -1, -0.75, \text{ and } -0.5$ ) of the time-averaged flow field, to show the regions of downwash produced by the vortical structures. In the isosurfaces of normalized  $Q$ , positive streamwise vorticity is colored in red (counterclockwise) and negative streamwise vorticity is colored in blue (clockwise), while the negative isosurfaces of

$v/U_\infty$  are colored green, with darker green showing larger downwash. This scheme is maintained for all similar plots in the present paper. Figure 9(a) shows the baseline case, Fig. 9(b) shows the full-chamfered pin, and Fig. 9(c) shows the half-chamfered pin. In both chamfered cases, the skew angle is  $\phi = 90^\circ$ , to highlight the unique features of the chamfered pins.

For the baseline case, similar features to those shown by Gildersleeve and Amitay [1] are also identified in Fig. 9(a). Consistent with the *OFV* result, two sets of horseshoe vortices are observable, with the first horseshoe vortex at around  $z^* = \pm 0.5$ , and a second horseshoe vortex at  $z^* = \pm 1$ . Secondary vortices are also visible between the horseshoe vortices. Between the sets of vortices, a symmetric region of downwash can be seen, around  $z^* = 0$ . This downwash is caused by the arch vortex and is important in terms of flow control as it helps in bringing momentum into the near wall region, as noted by Gildersleeve and Amitay [1]. Notably, in the near-wake, the regions of highest levels of downwash, seen as the innermost contours, show a two-lobed shape, corresponding to the shape of the arch vortex. Downstream, the region of downwash is also affected by the induced velocity of the inner horseshoe vortices. The magnitude of the downwash decreases with downstream and it diminishes by  $x^* = 3.5$ . The diminishing of the downwash is due to the dissipation of the arch vortices with downstream distance. Throughout the center region, small pockets of rotation are visible but no coherent pair of trailing vortices are distinguishable at these levels of  $Q$ .

Figures 9(b) and 9(c) show the same isosurfaces of normalized  $Q$  and contours of  $v/U_\infty$  for the flow past the full-chamfered pin and the half-chamfered pin, respectively, at  $\phi = 90^\circ$ . Like the baseline case, the wake of the full-chamfered pin [Fig. 9(b)] also shows the presence of two pairs of horseshoe vortices. However, the inner horseshoe on the  $z^* < 0$  side (the bottom of the chamfer) is smaller. Additionally, the outer pair of horseshoe vortices is barely visible at the level of  $Q$  utilized, showing as streaks of disconnected clusters of vorticity. Most importantly, in the center of the wake, the pair of trailing vortices described by Gildersleeve and Amitay [1] has been replaced by a different pair of vortices. While the trailing vortices in nonchamfered pins corotate with the horseshoe vortices on each side of the pin [1,15], this new pair of vortices are counter-rotating with respect to the horseshoe vortices. This pair of vortices is a unique feature created due to the addition of the chamfer, and as such referred to here as “chamfer-induced vortices” or CIVs. The CIV pair is also asymmetric, with a smaller positive vortex on the positive  $z^*$  side and a much larger negative vortex towards the negative- $z^*$  side. The smaller CIV decays by  $x^* = 2.25$  and is not visible at this level of  $Q$ . Meanwhile, the larger CIV is visible throughout the measurement domain. The single dominant CIV gives the chamfered pin at  $\phi = 90^\circ$  the qualities of a combined circular pin and a vortex generator. All the structures dissipate as they move downstream, leading to decreasing levels of vorticity at  $x^* = 3, 4$ , and  $5$ . Around the CIVs, the contours of downwash have also changed. The downwash region becomes asymmetric, with unequal lobes of high downwash on either side of the centerline from  $x^* = 1$  to  $x^* \approx 2$ . In fact, the contours for  $v/U_\infty \leq -1$  become two disconnected regions. The wake is skewed towards the chamfer side and the velocities are higher on the negative  $z^*$  side of the wake and the region of downwash on the positive  $z^*$  side is of a lower magnitude than the corresponding region in the baseline case. This is a result of the slanted free end, which causes an asymmetric separation bubble over the free end of the pin, which in turn causes the asymmetric downwash, as was also seen in the corresponding oil flow visualization in Fig. 8. This difference in velocity causes rotation around a point located near the pin’s centerline, leading to a strong negative CIV and a comparatively weaker positive CIV. The effect of this asymmetry was already seen in the *OFV* section, as the oil line between the two vortices, marked as (5), was skewed towards the chamfer. Since the CIVs rotate opposite to what was seen for the baseline, the regions of higher downwash occur between the CIVs and the horseshoes for the chamfered pins. This is different from the nonchamfered pin, where the downwash is between the two trailing vortices.

The stronger rotation on the larger, dominant CIV causes the downwash to sustain further downstream, with the selected contours ending at approximately  $x^* = 4.5$ . Thus, this system pulls flow towards the surface and adds vorticity to the near-wall region, which can be useful for flow control applications.

The flow past the half-chamfered pin [Fig. 9(c)] shows a similar structure pattern to that of the full-chamfered pin. Like the full-chamfered pin, two pairs of horseshoe vortices are visible at the selected level of  $Q$ . However, while the outer pair of horseshoe vortices in the full-chamfered pin is barely visible, in the case of the half-chamfered pin it is clearly distinguishable. The inner pair of the horseshoe vortices is also larger than for the full-chamfered case. Near the centerline ( $z^* = 0$ ), an asymmetric CIV vortex pair is also observed. The asymmetry between the two vortices is even more pronounced for the half-chamfered pin, with a noticeably larger negative CIV and a much smaller, shorter-lived positive CIV. Relative to the full-chamfered pin, the half-chamfered pin produces a notable increase downwash downstream of the pin, particularly on the side of the pin that is not chamfered. This is a result of even greater asymmetry in the separation, with the nonchamfered side producing a separation bubble similar to the baseline case, which produces a stronger downwash that strengthens the CIV on that side, while the shorter and steeper slanted side produces a weaker opposite vortex. This produces the system seen in Fig. 9(c), where the dominant CIV is larger than that of the full-chamfered pin and by far the largest vortex in the flow field. These structures gradually dissipate as they advect downstream. However, the contour of  $v/U_\infty = -0.5$  is still present at the final plane of  $x^* = 5$ .

To further explore the effect of the chamfer on the vortical structures in the wake, selected spanwise planes of the time-averaged in-plane velocity vectors, superimposed with contours of  $Q$  ( $Q = 0.012$ ), smoothed with a disk filter of  $R = 3$ , and colored by normalized streamwise vorticity, are shown in Fig. 10. The rows of Fig. 10 correspond to constant values of  $x^*$ ,  $x^* = 1$  [Figs. 10(a)–10(c)],  $x^* = 2$  [Figs. 10(d)–10(f)],  $x^* = 3$  [Figs. 10(g)–10(i)],  $x^* = 4$  [Figs. 10(j)–10(l)], and  $x^* = 5$  [Figs. 10(m)–10(o)]. Figures 10(a), 10(d), 10(g), 10(j), 10(m) correspond to the baseline case, Figs. 10(b), 10(e), 10(h), 10(k), 10(n) correspond to the full-chamfered pin, and Figs. 10(c), 10(f), 10(i), 10(l), 10(o) correspond to the half-chamfered pin. The freestream direction in these figures is outwards from the page. For the chamfered pins  $\phi = 90^\circ$  with the higher side is on the right of the images.

For the baseline pin, at  $x^* = 1$  [Fig. 10(a)], only the second horseshoe vortex pair (marked as HS 2) is observed near  $z^* = \pm 1$ , while one arm of the third horseshoe is visible in this level of  $Q$  (HS 3). Between the horseshoe vortices, the symmetric region of downwash seen on Fig. 9(a) is visible, showing two concentrations of vorticity (marked as AV) of the opposite sign as the horseshoe vortices. These correspond to the bending of the arch vortex into the flow, resulting in a streamwise component of vorticity, as seen by Gildersleeve and Amitay [1]. This region of downwash is important in terms of flow control as it helps in bringing momentum into the boundary layer, as also noted by Gildersleeve and Amitay [1]. At  $x^* = 2$  [Fig. 10(d)], the inner horseshoe has become visible near  $z^* = \pm 0.5$  and the flow field consists of the two pairs of horseshoe vortices (the now-visible HS 1 and the previously marked HS 2) together with two counter-rotating trailing vortices near the centerline, marked as TV. These trailing vortices are the small concentrations of vorticity observable at  $x^* = 2$  in the isosurface of Fig. 9(a). All the structures dissipate as they advect downstream, leading to decreasing levels of vorticity at  $x^* = 3, 4,$  and  $5$  [Figs. 10(g), 10(j), and 10(m), respectively). Correspondingly, the velocity magnitudes are smaller around the horseshoe vortices, as well as in the downwash region.

For the full-chamfered pin at  $x^* = 1$  [Fig. 10(b)], the flow field consists of two pairs of asymmetric horseshoe vortices (marked as HS 1 and HS 2), and a pair of asymmetric CIVs. The flow field is skewed to the left and the magnitude of the in-plane velocities are higher on the right side of the wake, all as a result of the slanted free end, where the varying immersion ratio along the span causes a skewed separation bubble, which in turn causes a skewed downwash distribution. This difference in velocity causes rotation around a point located near  $z^* = 0$ , leading to a stronger negative CIV and a comparatively weaker positive CIV. At  $x^* = 2$  [Fig. 10(e)], the flow field does not exhibit the two distinguishable pairs of horseshoe vortices, and the downwash region is dominated by the negative CIV, which has moved towards positive  $z^*$ . Farther downstream, at  $x^* = 3, 4,$  and  $5$  [Figs. 10(h), 10(k), and 10(n), respectively], similar trends are seen, consisting of a single horseshoe vortex and a CIV that progressively moves towards positive  $z^*$ . The horseshoe vortex is asymmetric, with

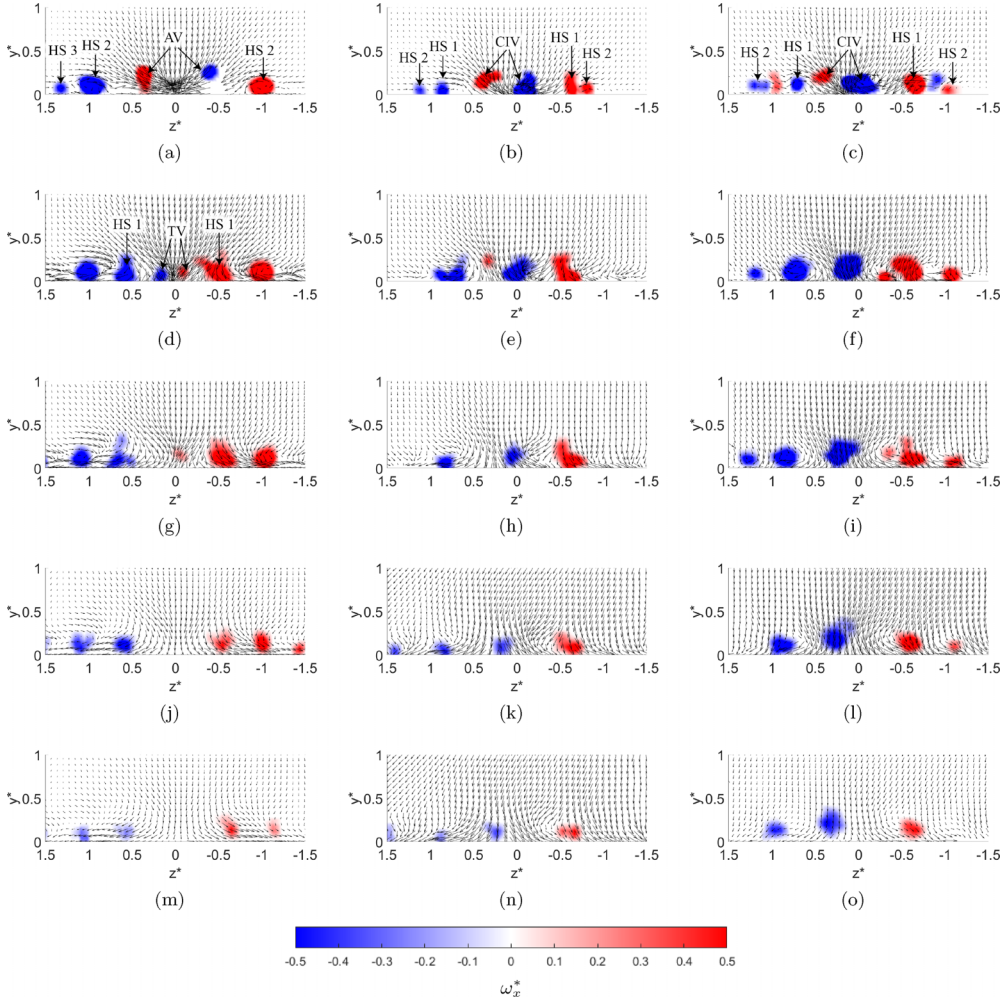


FIG. 10. Spanwise planes showing in-plane velocity vectors, superimposed with contours of  $Q$  ( $Q = 0.012$ ) colored by normalized streamwise vorticity, at (a)–(c)  $x^* = 1$ , (d)–(f)  $x^* = 2$ , (g)–(i)  $x^* = 3$ , (j)–(l)  $x^* = 4$ , and (m)–(o)  $x^* = 5$ . Baseline case (a), (d), (g), (j), (m), full-chamfered pin at (b), (e), (h), (k), (n)  $\phi = 90^\circ$ , and (c), (f), (i), (l), (o) half-chamfered pin. Both chamfered pins are at  $\phi = 90^\circ$ , and the flow direction is out of the page.

the vortex on the right-hand side being comparatively stronger. All the structures dissipate with downstream progression as expected. At  $x^* = 4$  and 5, small regions of vorticity concentrations are present at  $z^* \approx -1.5$ , which likely correspond to small weaker tertiary horseshoe structures.

For the half-chamfered pin at  $x^* = 1$  [Fig. 10(c)], the flow field also consists of a pair of asymmetric horseshoe vortices (HS 1 and HS 2) and a pair of asymmetric CIVs. In addition to these, a region of opposite vorticity is present between the two horseshoe vortices on each side, which corresponds to secondary horseshoe vortices induced by the main horseshoe vortices interacting with the wall. The downwash region around  $z^* = 0$  shows increased asymmetry compared with that of the full-chamfered pin in Fig. 10(b). This larger difference in velocity leads to an asymmetric CIV pair, with a stronger negative CIV and a weaker positive CIV. The dominant CIV is larger than that of the full-chamfered pin. This is because this pin has a larger portion of the free end at the highest immersion ration of  $\delta = 1.3$ , causing a higher difference in downwash between the

separated regions in the wall-parallel and slanted portions of the pin. This difference causes rotation. Farther downstream, at  $x^* = 2$  [Fig. 10(f)], the weaker CIV is not present at this  $Q$  level, nor is the secondary horseshoe vortex associated with the main horseshoe vortices, while the dominant CIV has migrated towards positive  $z^*$ . The CIV is also significantly larger than the full-chamfered pin and is also the largest vortex in the flow field. These structures gradually dissipate as they advect downstream [Figs. 10(i), 10(l), and 10(o)]. At the final plane of  $x^* = 5$  [Fig. 10(l)], only a single pair of small horseshoe vortex is seen together with a comparatively larger CIV.

To assess the strength and trajectory of the dominant CIV, the centroid of the CIV at different streamwise locations was found. MATLAB clustering algorithms were used to distinguish between the multiple observable vortices and identify their geometric centroids. Figures 11(a) and 11(b) show the downstream trajectories of the dominant CIV in the spanwise and wall-normal directions, respectively, for the two chamfered pins.

As can be seen, the dominant CIV from the full-chamfered pin is located at  $z^* \approx -0.2$  at  $x^* = 1$  and moves towards positive  $z^*$  (i.e., towards the chamfered side) as it progresses downstream, crossing the centerline ( $z^* = 0$ ) near  $x^* = 3.5$ . The dominant CIV associated with the half-chamfered pin starts closer to the centerline (at  $z^* \approx -0.1$  at  $x^* = 1$ ) and also moves towards positive  $z^*$  as it progresses downstream, crossing the centerline at  $x^* \approx 1.5$ . This behavior is explained by the interaction of the dominant CIV with the weaker CIV and the first pair of horseshoe vortices, with the dominant CIV moving towards corotating vortices and away from counter-rotating vortices through mutual induction. The interaction of the vortices with the wall also results in the trajectory of the CIV to the positive  $z^*$ . Throughout the measurement domain, the vortex generated by the half-chamfered pin is further towards the side that has the slanted surface, as a consequence of the higher asymmetry in the separation bubble over the free end of the pin discussed previously.

Figure 11(b) shows the vertical trajectory of the dominant CIV. The centroid of the dominant CIV generated by the half-chamfered pin is located farther away from the surface compared with the full-chamfered pin throughout the measurement domain. This is most likely due to the vortex being larger and the smaller angle of the chamfer, which consequently forces the center away from the wall. The centroid of the dominant CIV from the full-chamfered pin moves away from the wall in the near wake until  $x^* \approx 2.5$ , remains at a relatively constant distance from the wall until  $x^* \approx 3.3$ , then moves towards the wall showing another plateau as the interaction with the wall limits the movement towards it. This movement of the centroid towards the wall corresponds to the decay of the CIV seen in Fig. 10(k) and 10(n), as the vortex moves closer to the wall as the size of the vortex decreases. The dominant CIV from the half-chamfered pin also moves away from the wall at first until  $x^* \approx 2.17$ , where it reaches a plateau. These trajectories are dictated by the induction from the neighboring vortices and the downwash behind the pin. The movement away from the wall, which both CIVs exhibit between  $x^* = 1$  and  $x^* \approx 2.5$  can be correlated to the presence and decay of the weaker CIV, which can be seen in Fig. 9. This is because the weaker CIV and the dominant CIV form a pair of counter-rotating vortices, which ascend as a result of their mutual induction.

Figure 11(c) shows the downstream variation of the normalized streamwise circulation for the dominant CIV generated by each chamfered pin at  $\phi = 90^\circ$  defined as

$$\Gamma_x^* = \iint_{Q=0.012} \omega_x^* dz^* dy^*. \quad (3)$$

The circulation is shown as a scatter plot with a mean-square exponential trend line. As can be seen, the CIV from the half-chamfered pin is stronger throughout the measurement domain, as can also be observed visually from the contours of the vorticity levels in Fig. 9. As such, the half-chamfered pin shows more promise as a flow control actuator in terms of circulation addition to the flow. The circulation associated with the CIV from both pins decreases monotonically with downstream distance due to dissipation.

Next, the effect of the chamfer on the streamwise and wall-normal velocity profiles is presented in Fig. 12. Figures 12(a) and 12(b) show selected profiles at different streamwise location of streamwise and wall-normal velocity components, respectively, at the centroid of the dominant



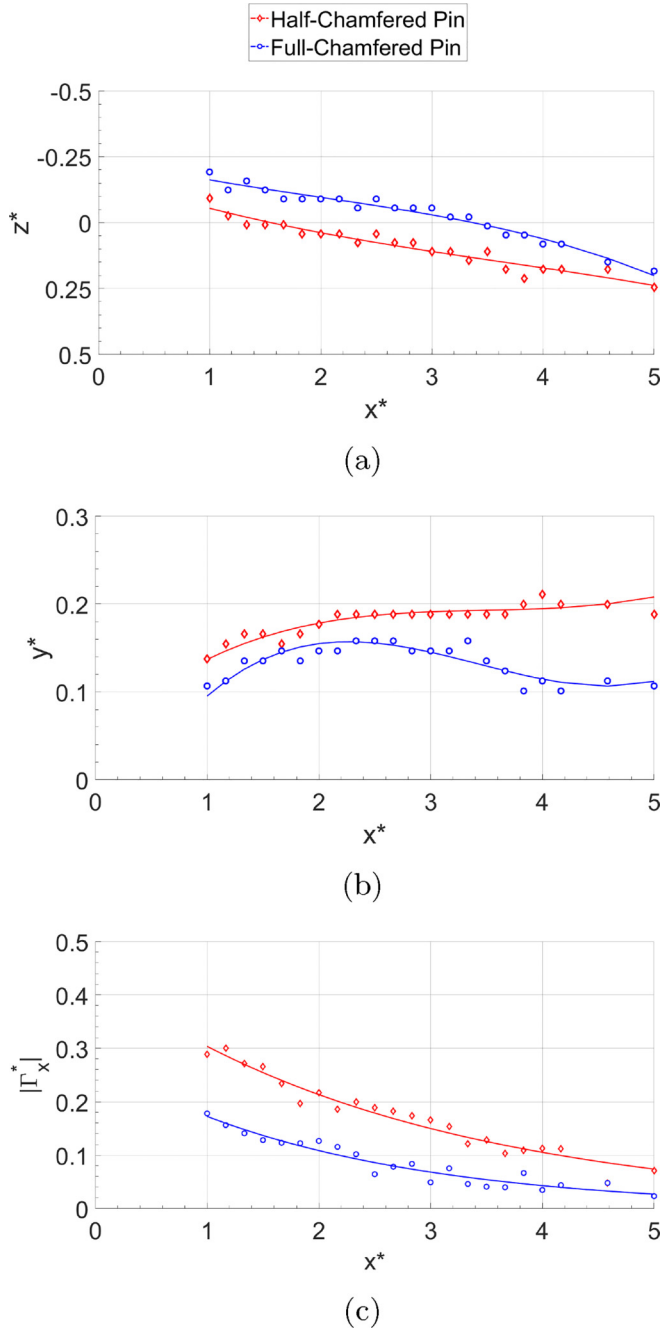


FIG. 11. (a) Spanwise trajectory, (b) wall-normal trajectory, and (c) normalized streamwise circulation,  $\Gamma_x^*$  of the dominant CIV generated by the two chamfered pins at  $\phi = 90^\circ$ .

CIV for pinless boundary layer (no pin present), the half-chamfered pin and full-chamfered pin. For the streamwise velocity profiles [Fig. 12(a)], the half-chamfered pin is represented in red on the top and the full-chamfered pin is seen in blue on the bottom. The lines with hollow symbols show the velocity profiles for the chamfered pins, the black lines represent the boundary layer profile at

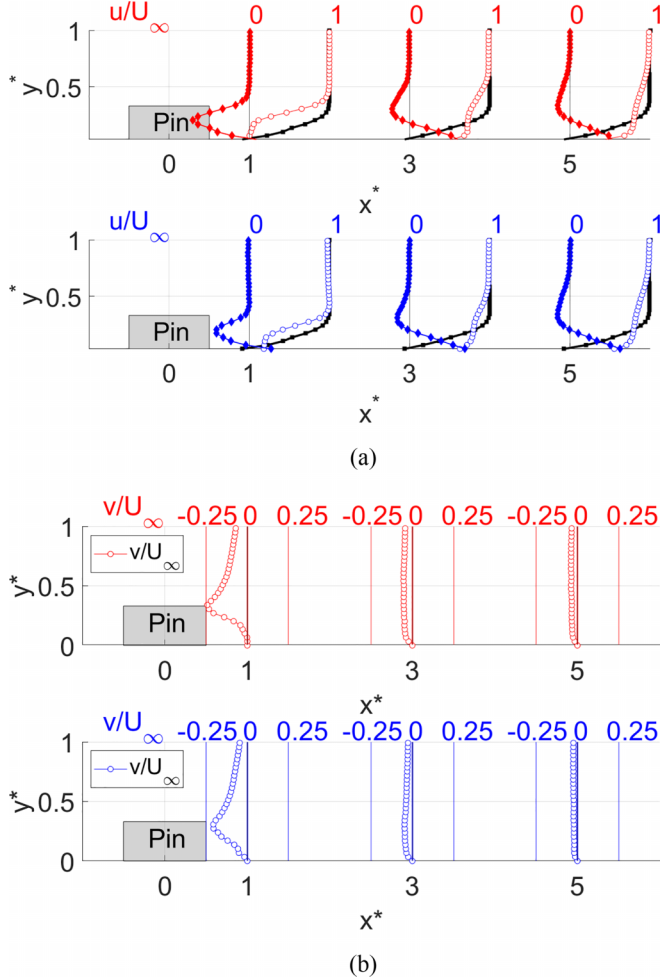


FIG. 12. Streamwise evolution of (a)  $u/U_\infty$ , and (b)  $v/U_\infty$  velocity profiles for the half-chamfered (red) and full-chamfered (blue) pins at  $\phi = 90^\circ$ , compared with the boundary layer profile without the pin, through the centroid of the dominant CIVs.

the corresponding location (without the pin), and the lines with solid symbols show the difference between the two profiles. The colored numbers over each plot show the velocity scales for each profile, and the zero velocity grid line is also the normalized streamwise location of the profile. The outline of the pin is shown at each location for comparison and context. For both chamfered pins, at  $x^* = 1$ , the streamwise velocity exhibit an inflection point, which is further away from the wall for the half-chamfered pin. Furthermore, the difference in the streamwise velocity between the chamfered and baseline boundary layer is negative throughout the boundary layer due to the separation behind the pins, where the larger deficit is for the half-chamfered pin. At  $x^* = 3$  and  $x^* = 5$ , the velocity profiles are fuller compared with  $x^* = 1$ , and there is higher velocity (compared with the baseline boundary layer) near the wall with a higher velocity gradient, suggesting added momentum near the wall and increased wall shear stress.

Figure 12(b) shows the wall-normal profiles of the normalized wall-normal velocity component through the centroid of the dominant CIV. As before, the half-chamfered pin is presented in red on the top row and the full-chamfered pin is seen in blue on the bottom row. The figure shows that both

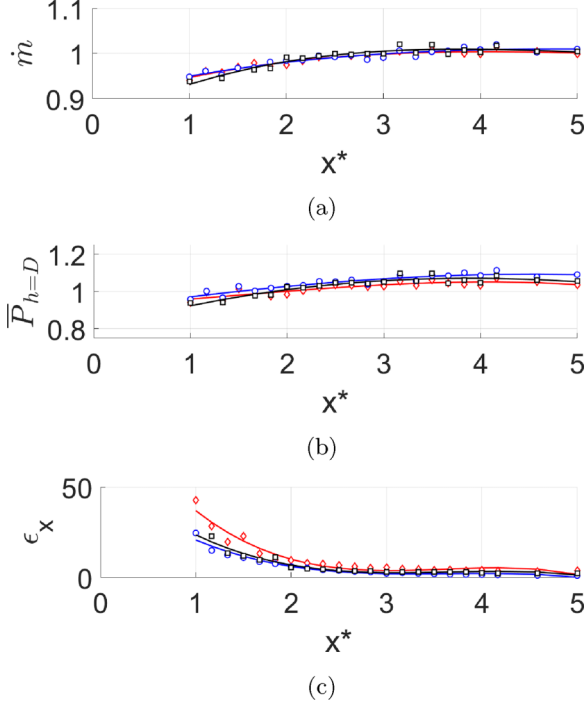


FIG. 13. Downstream evolution of the (a) mass flux  $\dot{m}^*$ , (b) added momentum  $\bar{P}^*$ , and (c) enstrophy  $\epsilon_x^*$  for the baseline pin, half-chamfered pin, and full-chamfered pin at  $\phi = 90^\circ$ .

CIVs produce downwash, particularly in the near-wake, with the effect dissipating downstream. The half-chamfered pin's CIV shows a larger level of downwash, where the maximum downwash occurs further away from the wall, consistent with the higher location of the vortex seen in Fig. 11(b). At  $x^* = 1$ , the largest downwash is located below the free-end for both pins, with the half-chamfered pin showing the peak at  $y^* = 0.32$ , and the full-chamfered pin showing the peak at  $y^* = 0.26$ . In both cases, this is further away from the wall than the centroid of the CIV.

To further explore the effect of chamfering, the streamwise evolution of the mass flux, added momentum into the boundary layer, and enstrophy, for the baseline pin, half-chamfered and full-chamfered pins at  $\phi = 90^\circ$  are presented in Fig. 13. The dimensionless streamwise mass flux  $\dot{m}^*$  is the quotient of the velocity at each point and the velocity of the pinless boundary layer flow, averaged along the span, which extends from  $z^* = -1.5$  to  $z^* = 1.5$  and from  $y^* = 0$  to  $y^* = 1$ . It is calculated as shown in Eq. (4):

$$\dot{m}^* = \int_{z_{\min}^*}^{z_{\max}^*} \int_0^1 \left( \frac{u}{u_B} \right) dy^* dz^*, \quad (4)$$

where  $u_B$  is the value of the streamwise velocity of the pinless boundary layer at a given  $(x^*, y^*, z^*)$  location. The added momentum into the boundary layer is a measure of flow separation resilience [23]. This near-wall momentum  $\bar{P}^*$  is calculated for a region from the wall to a height equal to the pin's diameter, and averaged along the span.  $\bar{P}^*$  at each downstream location along  $x^*$  is calculated as seen in Eq. (5):

$$\bar{P}^* = \int_{z_{\min}^*}^{z_{\max}^*} \int_0^1 \left( \frac{u^2}{u_B^2} \right) dy^* dz^*. \quad (5)$$

Finally, the enstrophy indicates enhanced mixing and turbulence, which represents the strength in vorticity [24] and is calculated over the entire domain as shown in Eq. (6). Note that all three values shown in Fig. 13 are integrated over an area that reaches outside of the boundary layer ( $4\delta$ ), which represents the global effects of the pin on the flow field:

$$\epsilon_x^* = \frac{1}{2} \int_{z_{\min}^*}^{z_{\max}^*} \int_0^1 (\omega_x^*)^2 dy^* dz^*. \quad (6)$$

In the near wake, for all the pins, compared with the pinless boundary layer, there is a reduction in mass flux due to separation behind the pin, an expected behavior from a flow around a bluff body cantilevered into the flow. The chamfered pins cause slightly smaller mass flux deficit in the near field, since they have smaller frontal areas compared with the baseline pin. Farther downstream, the normalized momentum flux associated with all three pins converges to the pinless boundary layer mass flux as the vortices dissipate. Similar trends can also be seen in the momentum added into the boundary layer. All pins cause a slight deficit of streamwise momentum in the near wake due to the blockage of the pins to the flow, with the full-chamfered pin causing the smallest deficit and the nonchamfered pin causing the largest. Downstream, all the pins actually add momentum into the near-wall region, with the full-chamfered pin adding the most and the half-chamfered pin adding the least. The trend of the streamwise momentum is opposite that of the enstrophy, particularly in the near wake, where the large vortical structures seen in Fig. 9(c) produce the highest level of vorticity and mixing. Downstream, the enstrophy for all three pins decreases monotonically as the vortical structures dissipate.

The downstream evolution of the streamwise component of the normalized circulation integrated over the entire data plane,  $\Gamma_{x\text{Total}}^*$ , and over each half of the plane separated at the centerline,  $\Gamma_{x\text{Half}}^*$ , are shown in Figs. 14(a) and 14(b), respectively, for each of the pins. These circulations were obtained using Eqs. (7a) (entire data plane) and (7b) (for  $z^* < 0$  and  $z^* > 0$ ):

$$\Gamma_{x\text{Total}}^* = \int_{z_{\min}^*}^{z_{\max}^*} \int_0^1 (\omega_x^*) dy^* dz^*, \quad (7a)$$

$$\Gamma_{x\text{Half}}^* = \int_{z_{\min}^*}^0 \int_0^1 (\omega_x^*) dy^* dz^*, \quad (7b)$$

$$\Gamma_{x\text{Half}}^* = \int_0^{z_{\max}^*} \int_0^1 (\omega_x^*) dy^* dz^*. \quad (7c)$$

Both chamfered pins (at  $\phi = 90^\circ$ ) have the net effect of adding negative circulation into the flow with respect to the baseline pin, which is due to the generation of the CIVs. This effect gradually decreases with downstream progression. Figure 14(b) shows that the full-chamfered pin decreases the absolute value of circulation on each half of the plane in comparison to the baseline pin, with the reduction being the largest closer to  $x^* = 1$ , and decreasing thereafter. The circulation for the full-chamfered pin on the  $z^* < 0$  side starts negative and becomes positive around  $x^* = 1.6$  while the circulation on the  $z^* > 0$  side stays negative throughout, which corresponds to the spanwise location of the CIVs at  $x^* = 1$ .

Meanwhile, the half-chamfered pin adds vorticity to the flow by increasing the absolute value of circulation on each half of the plane. This increase is small at  $x^* = 1$ , but the circulation from the half-chamfered pin grows at a faster rate between  $x^* = 1$  and  $x^* = 2$ , where the difference increases, and then converges to similar values as those seen for the baseline pin. This supports the previously discussed flow fields associated with the two chamfered pins.

It must be noted that the flow field around the pins are unsteady due to flow separation around them, resulting in shedding of vortical structures into the flow. Therefore, in addition to exploring the effect of the chamfer on the time-averaged flow field, the effect on the unsteadiness of the flow also needs to be discussed. Figures 15(a)–15(c) show isosurfaces of normalized  $Q$  ( $Q = 0.012$ ), colored by  $TKE^*$ , for the baseline pin, the full-chamfered pin, and the half-chamfered pin, respectively.

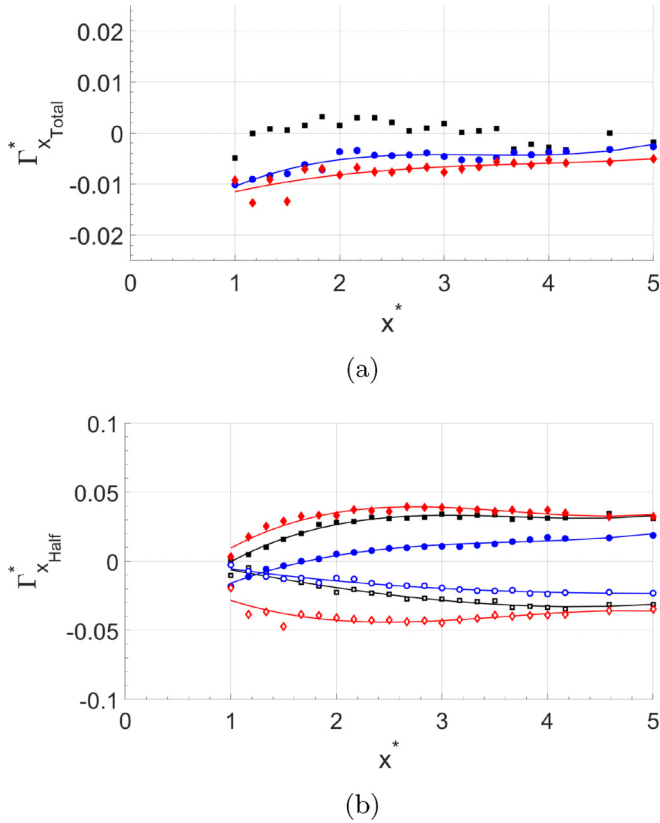


FIG. 14. Downstream evolution of the streamwise component of (a) the normalized streamwise circulation of the entire plane  $\Gamma_{x_{Total}}^*$  and (b) circulation on each half of the plane ( $\Gamma_{x_{Half}}^*$ ) for the two chamfered pins at  $\phi = 90^\circ$  and the baseline pin.

For the baseline pin, the highest levels of  $TKE^*$  are observed in the recirculation region and the trailing vortices around the center of the wake (around  $z^* = 0$ ). For the chamfered pins, the maximum  $TKE^*$  occurs on the CIVs between  $x^* = 1$  and  $x^* = 3$ . This is the same region where the highest levels of downwash were observed in Figs. 9(b) and 9(c), which is consistent with the asymmetric separation bubble rolling into the CIVs. This is also where the dominant and the

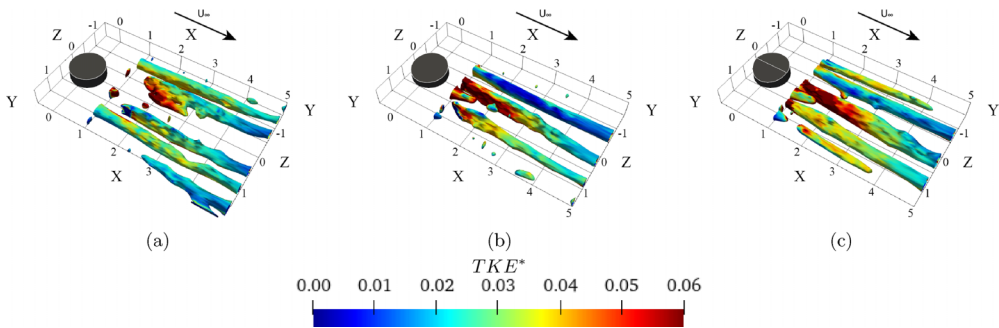


FIG. 15. Isosurfaces of normalized  $Q$  ( $Q = 0.012$ ), colored by  $TKE^*$ , for (a) the baseline pin, (b) the full-chamfered pin, (c) and the half-chamfered pin. The chamfer is at  $\phi = 90^\circ$ .

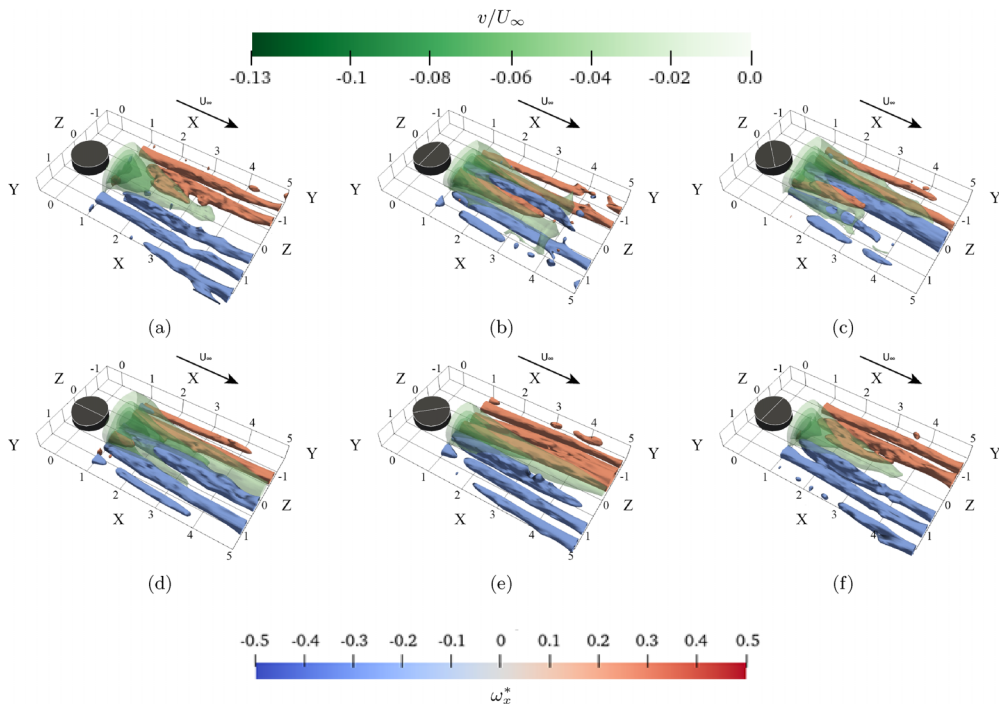


FIG. 16. Isosurfaces of normalized  $Q$  ( $Q = 0.012$ ), colored by normalized streamwise vorticity, and superimposed with contours of normalized wall-normal velocity. Half-chamfered pin at different skew angles of (b)  $\phi = 0^\circ$ , (c)  $45^\circ$ , (d)  $90^\circ$ , (e)  $135^\circ$ , and (f)  $180^\circ$ . The case for the (a) nonchamfered pin is also shown for comparison.

weaker CIVs interact with each other. Downstream of this region, the unsteadiness of the dominant CIV is reduced, which is associated with the reduced levels of  $TKE^*$ . It is also noted that for both chamfered pins, the horseshoe vortices on the  $z^* > 0$  (towards the chamfer) side exhibit higher  $TKE^*$  levels than those on the  $z^* < 0$  side, especially for the fully chamfered pin. This is due to the interactions between the inner horseshoe vortices and the near wake observed in Fig. 8. In general, the chamfered pins produce higher  $TKE^*$ , suggesting higher mixing, which may lead to more effective flow control.

Since the half-chamfered pin shows a greater effect on the flow field, the rest of the paper will be focused on this pin.

## 2. Effect of the skew angle: Half-chamfered pin

Next, the effect of the chamfer's skew angle on the flow field behind the half-chamfered pin and the associated vortical structures are explored. Figures 16(a)–16(f) show isosurfaces of normalized  $Q$  ( $Q = 0.012$ ) colored by streamwise vorticity and superimposed with isosurfaces of  $v/U_\infty$  ( $v/U_\infty = -1.25, -1, -0.75, -0.5, 0.25, 0.5, 0.75, 1, 1.25$ ) for the nonchamfered pin, and the half-chamfered pin at  $\phi = 0^\circ$ ,  $\phi = 45^\circ$ ,  $\phi = 90^\circ$ ,  $\phi = 135^\circ$ , and  $\phi = 180^\circ$ , respectively. In all cases the data is time-averaged. Note that the baseline pin is included here to help the reader in direct comparison.

At a skew angle of  $\phi = 0^\circ$  [Fig. 16(b)], the half-chamfered pin produces two pairs of horseshoe vortices and a pair of large counter-rotating CIV pair. Note that these CIVs are counter-rotating with respect to the horseshoe vortices. The direction of rotation of these CIVs suggests that the flow is moving from the slanted surface of the pin towards its sides. This, along with the corresponding

*OFV* image (Fig. 8), suggests that the incoming flow impacts the slanted surface creating a stagnation region. This causes the pressure to be higher than on the surrounding cylindrical surface, leading to the formation of these vortices. As mentioned in the previous section for the case with  $\phi = 90^\circ$ , the direction of rotation of these vortices causes two separate regions of high downwash. The first region is composed of two lobes located between the two CIVs and the first pair of horseshoe vortices. The second region is over the two CIVs near  $x^* = 1$  and corresponds to the end of the recirculation region caused by the flow separation over the free end of the pin. The downwash from the recirculation region meets a very small region of upwash located near the wall between the two CIVs near  $z^* = 0$  (obstructed in the figure) which is caused by the counter-rotation of the two vortices.

As the slanted surface is rotated to  $\phi = 45^\circ$  [Fig. 16(c)], the vortices on the slanted side ( $z^* > 0$ ) become weaker and the vortices on the nonslanted side ( $z^* < 0$ ) become stronger. This is associated with the interaction between the angled separation line and the arch vortex shown in Fig. 8. With the separation line being located farther downstream towards  $z^* > 0$ , the space available on the free end of the pin for the separation bubble to develop and reattach changes. This also changes the separation angle off the trailing edge described by Gildersleeve and Amitay [1] where the arch vortex is present. The effect of these phenomena is a spanwise variation in the arch vortex. Downstream, the asymmetric arch vortex is associated with an asymmetric pair of CIVs. Note that at  $\phi = 0^\circ$ , the CIVs are of equal strength whereas at  $\phi = 45^\circ$  the negative CIV is significantly stronger and last farther downstream than the positive CIV. Thus, a single dominant CIV starts to develop on the opposite half of the plane with respect to the slanted surface.

Compared with the previously discussed case where  $\phi = 90^\circ$  [Fig. 16], the case where  $\phi = 45^\circ$  generates a downwash that decays faster along  $x^*$  on both sides of the pin. Additionally, the regions of higher downwash are smaller in both the wall-normal and spanwise directions. An additional concentration of downwash can be seen on the far  $z^* > 0$  side of the wake as a result of interactions between the horseshoe vortices.

At  $\phi = 90^\circ$  [Fig. 16(d)], it can now be observed that the positive CIV on the slanted side diminishes faster than for  $\phi = 45^\circ$ , leaving a single dominant CIV. However, the dissimilarity between the strengths of the horseshoe vortices observed at  $\phi = 45^\circ$  is no longer clear. The horseshoe vortices at  $\phi = 90^\circ$  are also larger than at  $\phi = 45^\circ$ , making them more comparable to the dominant CIV. The corresponding *OFV* in Fig. 8 shows a surface topology similar to the baseline case, as was also seen by Gildersleeve and Amitay [1] and Roh and Park [16], which suggests that each spanwise half individually follows a similar structure to the baseline case. The CIV pair, in this case, is generated by the asymmetry in the mushroom-type vortex caused by the different angles of the two surfaces.

The flow field changes dramatically when the skew angle is increased to  $\phi = 135^\circ$  [Fig. 16(e)], where the slanted surface is on the wake side. Unlike the CIVs seen in the previous two cases, the directions of rotation of the vortices in the center of the wake have changed to corotating with respect to the horseshoe vortices. The change in direction of rotation of the vortices suggests that the chamfer being on the wake side generates a vortical system and pressure distribution more similar to the baseline case, which generates trailing vortices that corotate with the horseshoes on either side. This result is consistent with the corresponding *OFV* image, where an oil concentration around the most upstream point of the slanted surface was seen. This oil concentration is indicative of flow separation, which would favor rotation around the edge of the pin in the direction observed in this case. The CIV on the  $z^* < 0$  side merges with the inner horseshoe vortex on the same side. Because of the counter-rotating nature of the CIVs, such merging is not observed at the other skew angles. The outer horseshoe vortices are larger than at  $\phi = 0^\circ$  and  $45^\circ$ . Meanwhile, the region of downwash, as can be expected, is very different from the previous asymmetrical cases. The region of high downwash is located in the center of the wake between the CIVs and toward  $z^* < 0$  as a consequence of the CIVs advecting asymmetrically downstream as they interact with the horseshoe vortices. As before, and particularly as seen in the baseline case, the downwash is concentrated in the center, consistent with the oil accumulations from the legs of the arch vortex seen in the corresponding image in Fig. 8.

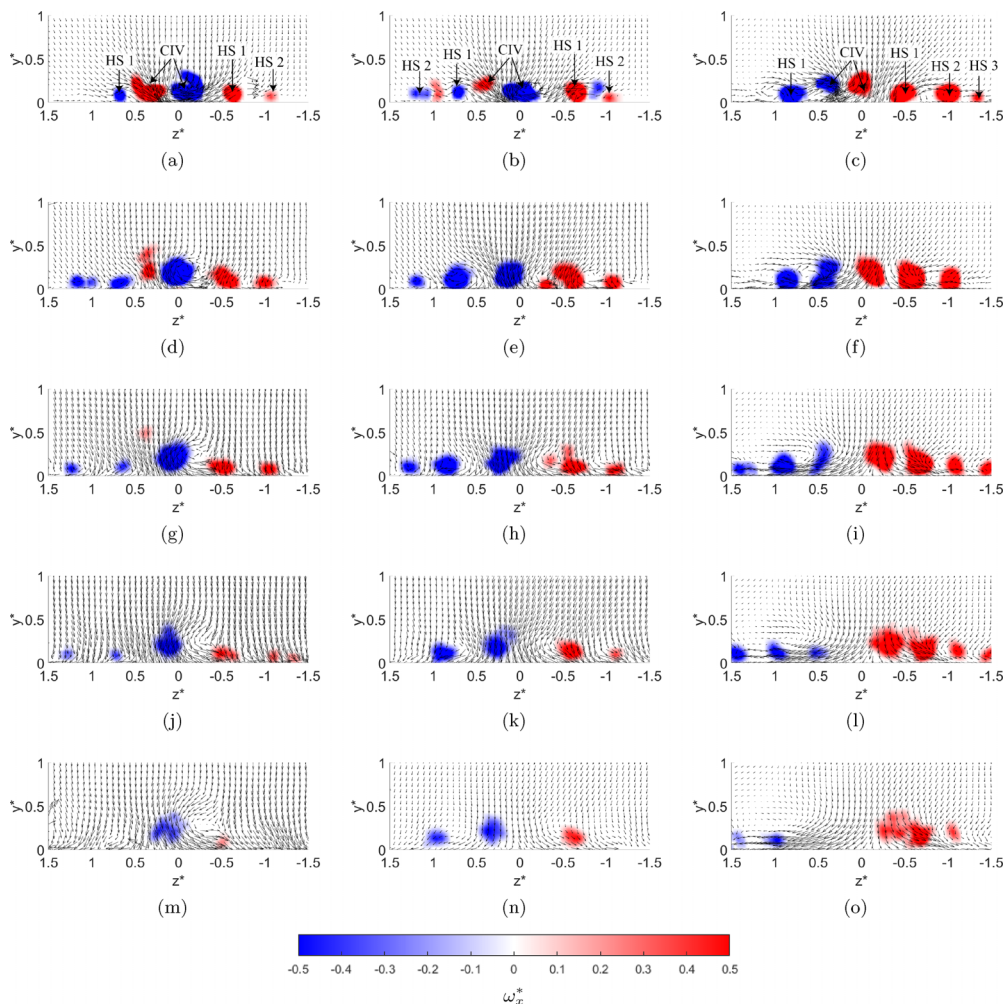


FIG. 17. Spanwise planes of in-plane velocity vectors, superimposed with contours of  $Q$  ( $Q = 0.012$ ), colored by normalized streamwise vorticity, at (a)–(c)  $x^* = 1$ , (d)–(f)  $x^* = 2$ , (g)–(i)  $x^* = 3$ , (j)–(l)  $x^* = 4$ , and (m)–(o)  $x^* = 5$  for the half-chamfered pin. (a), (d), (g), (j), (m)  $\phi = 45^\circ$ , (b), (e), (h), (k), (n)  $\phi = 90^\circ$ , and (c), (f), (i), (l), (o)  $\phi = 135^\circ$ . Flow is out of the page.

Finally, the flow field is examined when the pin is rotated to  $\phi = 180^\circ$  [Fig. 16(f)]. The wake resembles the baseline case in terms of the recognizable structures, except the vortices in the middle of the wake are strengthened by the presence of the slanted surface to a level where they are now distinguishable at the utilized levels of  $Q$ . This strengthening is a consequence of the larger separation bubble at the trailing edge of the pin, providing a larger pressure gradient, or alternatively of the wider legs of the arch vortex. Both of these features were noted in Fig. 8.

Figures 17(a)–17(o) show spanwise planes of time-averaged in-plane velocity vectors, superimposed with isosurfaces of normalized  $Q$  (also from the time-averaged flow field), colored by normalized streamwise vorticity and smoothed with a disk filter of  $R = 3$ . The results presented here are for the half-chamfered pin at selected downstream locations at skew angles of  $\phi = 45^\circ$ ,  $90^\circ$ , and  $135^\circ$ . The rows correspond to constant values of  $x^*$ , with  $x^* = 1$  [Figs. 17(a)–17(c)],  $x^* = 2$  [Figs. 17(d)–17(f)],  $x^* = 3$  [Figs. 17(g)–17(i)],  $x^* = 4$  [Figs. 17(j)–17(l)], and  $x^* = 5$  [Figs. 17(m)–17(o)]. Figures 17(a), 17(d), 17(g), 17(j), and 17(m) correspond to  $\phi = 45^\circ$ , Figs. 10(b), 10(e),



10(h), 10(k), and 10(n) correspond to  $\phi = 90^\circ$ , and Figs. 10(c), 10(f), 10(i), 10(l), and 10(n) correspond to  $\phi = 135^\circ$ . The freestream direction is out of the page, and the higher side of the chamfered pins is on the right side of the images.

When the pin is skewed to  $\phi = 45^\circ$  at  $x^* = 1$  [Fig. 17(a)] the flow field is asymmetric. The negative CIV is present near the mid-span, and the positive CIV is next to it on the  $z^* < 0$  side. At this streamwise location, both CIVs are of comparable size. The inner pair of horseshoe vortices (marked as HS 1) is visible at  $z^* \approx \pm 0.6$ , whereas of the outer pair (marked as HS 2) only the one on the  $z^* < 0$  side is detected at the selected level of  $Q$  and is seen around  $z^* \approx 1.1$ . At  $x^* = 2$  [Fig. 17(d)], the two pairs of horseshoe vortices can be seen, and the positive CIV has begun to decay and move away from the surface. The decay of the positive CIV in turn has allowed the negative CIV to grow and move such that it is approximately at the mid-span. The same trend is seen at  $x^* = 3, 4,$  and  $5$  [Figs. 17(g), 17(j), and 17(m), respectively]. The weaker positive CIV is no longer visible after  $x^* = 3$ , and the dominant negative CIV has moved to the  $z^* > 0$  side of the mid-span and dominates the flow field.

The case with  $\phi = 90^\circ$  [Figs. 10(b), 10(e), 10(h), 10(k), 10(n)] was discussed before and is shown here for reference. When the skew angle is increased to  $\phi = 135^\circ$ , the flow field is very different from the other two skew angle cases. At  $x^* = 1$  [Fig. 17(c)], the structures are similar to the baseline pin consisting of a well-defined set of vortices in the center of the wake, the CIVs, that are corotating with respect to the horseshoe vortices. However, the flow field is asymmetric due to the skew angle of the chamfer, which causes the positive vortex to be located near the centerline and the negative vortex to be near the spanwise end of the pin ( $z^* = 0.5$ ). The horseshoe vortices are more visible on the  $z^* < 0$  side, with three well-defined vortices observable (HS 1, HS 2, and HS 3), compared with only one on the  $z^* > 0$  side. Also, the inner pair of horseshoe vortices is asymmetric, with the vortex on the  $z^* < 0$  side at  $z^* \approx 0.5$  and the vortex on the  $z^* > 0$  side between  $z^* = -0.5$  and  $z^* = -1$ . The small positive vortex at  $z^* \approx -1.4$  is a weak tertiary structure, which is also observed at  $x^* = 3$  and  $4$ . The second negative horseshoe vortex on the  $z^* > 0$  side is not observed as it is weak and fragmented, as also observed in Fig. 16(e).

At  $x^* = 2$  [Fig. 17(f)], the two CIV move away from each other and from the centerline, while no significant change is observed in the positions of the horseshoe vortices. At  $x^* = 3$  [Fig. 17(i)], the second negative horseshoe vortex on the  $z^* > 0$  is observable. At  $x^* = 4$ , the positive CIV starts merging with the inner horseshoe vortex and the two are completely merged by  $x^* = 5$ . This was also seen in Fig. 8. All the structures diffuse and move away from the centerline between  $x^* = 3$  and  $x^* = 5$ . At the last downstream plane, the  $z^* > 0$  side consists of two weak horseshoe vortices, and the negative CIV is too weak to be identified at this level of  $Q$ . On the  $z^* < 0$  side, there is the merged CIV-horseshoe vortex and a weak outer horseshoe vortex.

The downstream evolution of the streamwise component of the normalized circulation for the entire interrogation spanwise plane ( $\Gamma_{xTotal}^*$ ) and its two halves ( $\Gamma_{xHalf}^*$ ) are shown in Figs. 18(a) and 18(b), respectively, for the half-chamfered pin at the three skew angles previously discussed. The results for the nonchamfered pin are also included for comparison. When the skew angle is  $\phi = 45^\circ$  there is a net addition of negative circulation compared with the nonchamfered pin. However, the increase in the circulation with respect to the nonchamfered pin is smaller than that of the pin with a chamfer at  $\phi = 90^\circ$ . The pin at  $\phi = 45^\circ$  achieves this net nonzero circulation with respect to the nonchamfered pin by generating a smaller amount of circulation than the nonchamfered pin on the  $z^* < 0$  side, while the circulation on the  $z^* > 0$  side is approximately the same as the nonchamfered case. Meanwhile, when the skew angle is  $\phi = 135^\circ$ , there is a net effect of adding positive circulation to the flow. It is achieved by increasing the circulation on the  $z^* < 0$  side, to levels above those seen for the case with  $\phi = 90^\circ$ , while the circulation on the  $z^* > 0$  side is approximately the same as the nonchamfered pin. Overall, the addition of either positive or negative streamwise circulation can be obtained by changing the skew angle.

Finally, the effect of the skew angle on the flow unsteadiness is discussed using  $TKE^*$ . Figures 19(a)–19(f) show isosurfaces of normalized  $Q$  ( $Q = 0.012$ ) colored by  $TKE^*$  for the half-chamfered pin at the different skew angles. At  $\phi = 0^\circ$  and  $\phi = 45^\circ$ , the highest levels of

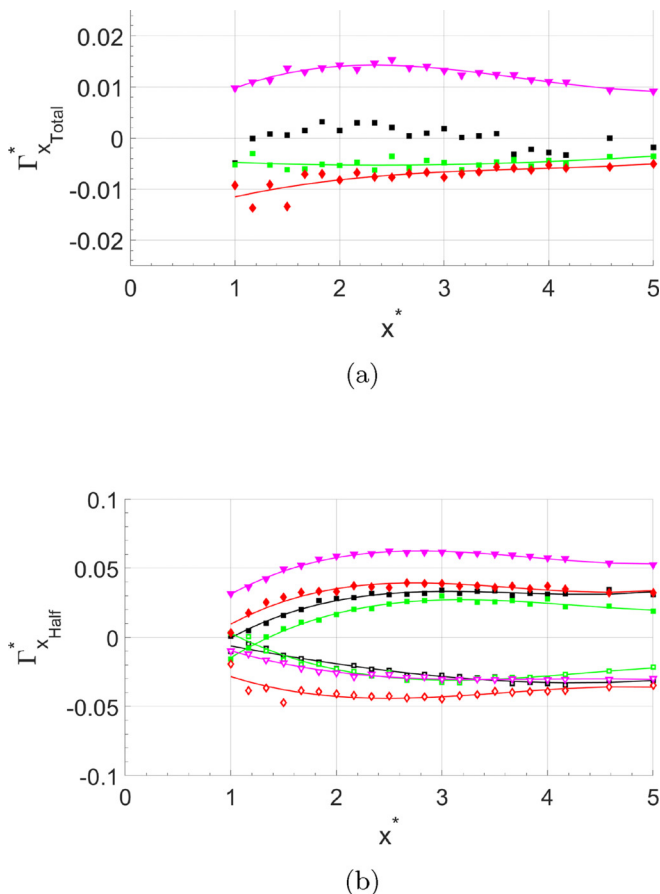


FIG. 18. Comparison of the (a) normalized streamwise circulation  $\Gamma_{x_{Total}}^*$  and (b) streamwise circulation on each side of the pin's centerline  $\Gamma_{x_{Half}}^*$  for the flow past the half-chamfered pin at  $\phi = 45^\circ$ ,  $90^\circ$ , and  $135^\circ$ . The corresponding circulation of the nonchamfered pin is also included for comparison.

$TKE^*$  are observed around the regions of the highest downwash, which is also the region where the interaction between the two CIVs occur. This region of high  $TKE^*$  exists approximately between  $x^* = 1$  and  $x^* = 3$ , becoming longer and narrower as the skew angle increases, in the same way as the downwash seen in Fig. 16.

For the cases where the slanted surface is on the wake side (i.e.,  $\phi = 135^\circ$  and  $\phi = 180^\circ$ ), the highest  $TKE^*$  is between the trailing vortices and the inner horseshoe vortices. This is just downstream of the region where the legs of the arch vortex were observed in Fig. 8. For these two cases, the peak  $TKE^*$  is lower and the high  $TKE^*$  region does not extend as far downstream as for the cases where the slanted surface is on the upstream side of the pin. For all cases, the  $TKE^*$  levels diminish rapidly away from the peaks. The low  $TKE^*$  levels at the end of the interrogation region suggest that these coherent vortices, including the merged trailing-horseshoe vortices for  $\phi = 135^\circ$ , become quasisteady by the end of the measurement domain.

#### IV. CONCLUSIONS

The interactions of cantilevered, low aspect ratio cylindrical pins having chamfered tops with a laminar boundary layer were explored experimentally. Three pins were investigated in this study, a pin where the slanted portion encompasses the diameter of the pin (referred to as the

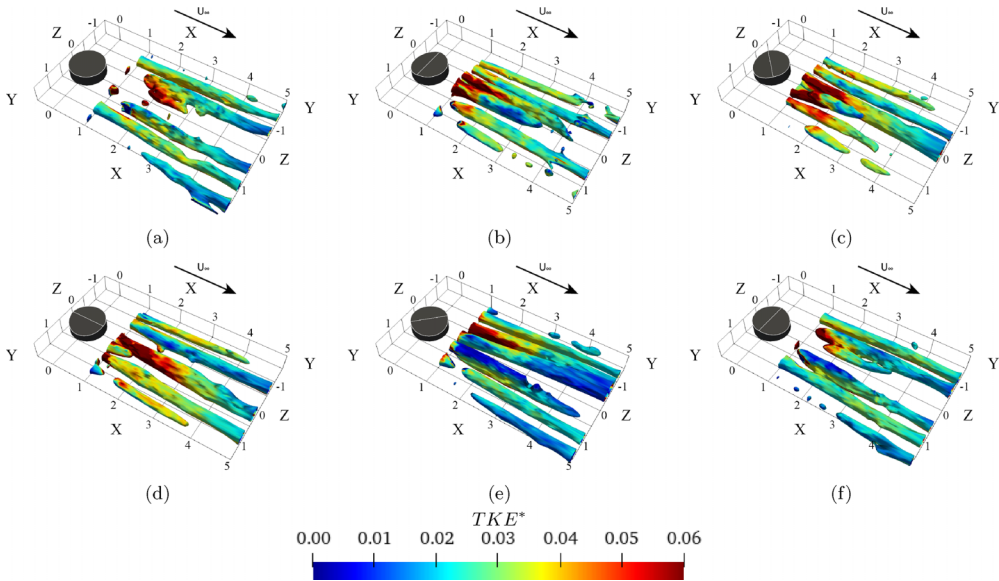


FIG. 19. Isosurfaces of normalized  $Q$  ( $Q = 0.012$ ), colored by  $TKE^*$ . Half-chamfered pin at skew angles of (b)  $\phi = 0^\circ$ , (c)  $45^\circ$ , (d)  $90^\circ$ , (e)  $135^\circ$ , and (f)  $180^\circ$ . The case for (a) the nonchamfered pin is also shown for comparison.

“full-chamfered” pin), a pin where the slanted portion encompasses half of the pin planform (referred to as the “half-chamfered” pin), and a nonchamfered pin that served as the baseline case. The investigation was performed using stereoscopic particle image velocimetry, at a Reynolds number (based on the pin diameter) of  $Re_D = 8 \times 10^3$ . The pins’ relative submergence was calculated based on the highest point of the pins and kept constant at  $h/\delta = 1.3$ .

It was shown that the chamfered pins show substantial promise in terms of generating strong streamwise vortices that can enhance flow control capabilities, by acting as a combination of a pin and a vortex generator depending on the skew angle between the slanted plane and the incoming flow. While several of the flow features associated with nonchamfered, low aspect ratio pin remain, the chamfer further increases the complexity of the flow field. Different asymmetric vortical structures and varying interactions occur, depending on the shape of the pin and its skew angle with respect to the incoming freestream. The most important of these features for the stated objective of this investigation are the large vortices referred to as the chamfer-induced vortices, or CIVs, which are produced due to the slanted surface at certain skew angles. Specifically, the chamfered pins produce these vortices when the slanted plane is facing into the flow (directly or at an angle), or facing perpendicular to the flow. The CIVs in this case rotate opposite to the trailing vortices seen in cylindrical low-aspect ratio pins and are primarily formed from the asymmetry of the arch vortex. When the chamfer faces directly into the flow, a symmetric pair of these vortices appear, and as the skew angle increases, the CIV located on the higher side of the chamfer becomes larger and dominates the flow field, which then resembles that produced by a vane-type vortex generator. Unlike a vortex generator, however, the presence of horseshoe vortices and the downwash over the pin produce an interaction that causes a streamwise migration of the CIVs towards the side that has the chamfer. The extent of this migration depends on the skew angle. When the slanted plane is facing away from the flow, the CIV vortical system changes, and instead, the resulting vortices in the center of the wake rotate in the direction of those seen for nonchamfered cylindrical pins, i.e., corotating with the horseshoe vortices. Because of this corotation, the CIVs immediately interact with the horseshoe vortices and move away from the centerline of the pin, producing a large

skewed downwash region in its wake. As the slanted region rotates such that its centerline aligns with the flow direction, the asymmetry is lost and the flow field resembles that of the cylindrical case, with the exception of showing weaker horseshoe vortices and stronger CIVs in the center of the wake. Additionally, the half-chamfered pin produces a higher magnitude of net circulation than the full-chamfered pin, as well as stronger CIVs. This is because the portion of the free end of the pin that is parallel to the floor produces a separation bubble which in turn produces downwash that augments the CIVs. Moreover, its flow field is associated with higher  $TKE^*$ .

Finally, it was observed that the chamfered pins produce a net increase in streamwise circulation. Furthermore, rotating the pins such that their slanted surface is skewed with respect to the flow can add positive or negative circulation depending on the skew angle. In that sense, these pins show promise as flow control devices in application where the simultaneous addition of both circulation and downwash is desirable. This approach can also be modified by rotating the pin to adapt to changes in flow direction, tailoring the size and orientation of the chamfer-induced vortex to the changing conditions.

#### ACKNOWLEDGMENT

This work is supported by the United States Office of Naval Research under the Grant No. N00014-20-1-2388.

- 
- [1] S. Gildersleeve and M. Amitay, Vortex dynamics of a low aspect ratio cantilevered cylinder immersed in a boundary layer, *J. Fluid Mech.* **901**, A18 (2020).
  - [2] D. Sumner, Flow above the free end of a surface-mounted finite-height circular cylinder: A review, *J. Fluids Struct.* **43**, 41 (2013).
  - [3] H. Sakamoto and M. Arie, Vortex shedding from a rectangular prism and a circular cylinder placed vertically in a turbulent boundary layer, *J. Fluid Mech.* **126**, 147 (1983).
  - [4] T. Kawamura, M. Hiwada, T. Hibino, I. Mabuchi, and M. Kumada, Flow around a finite circular cylinder on a flat plate: Cylinder height greater than turbulent boundary layer thickness, *Bull. JSME* **27**, 2142 (1984).
  - [5] N. Hölscher and H.-J. Niemann, Turbulence and separation induced pressure fluctuations on a finite circular cylinder-application of a linear unsteady strip theory, *J. Wind Eng. Ind. Aerodyn.* **65**, 335 (1996).
  - [6] D. Sumner, J. Heseltine, and O. Dansereau, Wake structure of a finite circular cylinder of small aspect ratio, *Exp. Fluids* **37**, 720 (2004).
  - [7] S. Okamoto and Y. Sunabashiri, Vortex shedding from a circular cylinder of finite length placed on a ground plane, *J. Fluids Eng.* **114**, 512 (1992).
  - [8] G. Palau-Salvador, T. Stoesser, J. Fröhlich, M. Kappler, and W. Rodi, Large eddy simulations and experiments of flow around finite-height cylinders, *Flow, Turbul. Combust.* **84**, 239 (2010).
  - [9] S. Gildersleeve and M. Amitay, Control of flow separation over a flapped airfoil using low-aspect-ratio circular pins, *AIAA J.* **57**, 628 (2019).
  - [10] T. A. Fox and G. West, Fluid-induced loading of cantilevered circular cylinders in a low-turbulence uniform flow. part 1: Mean loading with aspect ratios in the range 4 to 30, *J. Fluids Struct.* **7**, 1 (1993).
  - [11] R. Pattenden, S. Turnock, and X. Zhang, Measurements of the flow over a low-aspect-ratio cylinder mounted on a ground plane, *Exp. Fluids* **39**, 10 (2005).
  - [12] S. Gildersleeve, D. Clingman, and M. Amitay, Separation control over a flapped NACA 0012 model using an array of low aspect ratio cylindrical pins, in *8th AIAA Flow Control Conference* (2016), p. 4088.
  - [13] S. Gildersleeve, B. A. Tuna, and M. Amitay, Interactions of a low-aspect-ratio cantilevered dynamic pin with a boundary layer, *AIAA J.* **55**, 2142 (2017).
  - [14] H. M. Shehata and A. Medina, The wake structure of a stationary and a rotary wall-mounted low-aspect-ratio cylinder, *AIAA J.* **59**, 4815 (2021).

- [15] S. M. Gildersleeve, Ph.D. thesis, Rensselaer Polytechnic Institute, 2018 (unpublished).
- [16] S. Roh and S. Park, Vortical flow over the free end surface of a finite circular cylinder mounted on a flat plate, *Exp. Fluids* **34**, 63 (2003).
- [17] C. Baker, The laminar horseshoe vortex, *J. Fluid Mech.* **95**, 347 (1979).
- [18] C. Baker, The turbulent horseshoe vortex, *J. Wind Eng. Ind. Aerodyn.* **6**, 9 (1980).
- [19] J. H. Agui and J. Andreopoulos, Experimental investigation of a three-dimensional boundary layer flow in the vicinity of an upright wall mounted cylinder (data bank contribution), *J. Fluids Eng.* **114**, 566 (1992).
- [20] B. Wieneke, PIV uncertainty quantification from correlation statistics, *Meas. Sci. Technol.* **26**, 074002 (2015).
- [21] A. Sciacchitano and B. Wieneke, PIV uncertainty propagation, *Meas. Sci. Technol.* **27**, 084006 (2016).
- [22] T. Tsutsui and M. Kawahara, Heat transfer around a cylindrical protuberance mounted in a plane turbulent boundary layer, *J. Heat Transfer* **128**, 153 (2006).
- [23] D. R. Smith, Interaction of a synthetic jet with a crossflow boundary layer, *AIAA J.* **40**, 2277 (2002).
- [24] D. A. Compton and J. P. Johnston, Streamwise vortex production by pitched and skewed jets in a turbulent boundary layer, *AIAA J.* **30**, 640 (1992).